Biomedicine & Pharmacotherapy 201 (2026) 119727

Contents lists available at ScienceDirect

Biomedicine & Pharmacotherapy

journal homepage: www.elsevier.com/locate/biopha

Photocontrol of zebrafish behavior with a photoswitchable ligand of nicotinic acetylcholine receptors

Claudio Papotto [a], Nayeli Fernanda Pérez-Pérez [b,c,d], Alexandre M.J. Gomila [b,c,1], Rosalba Sortino [b,c], Mercè Cases [e], Hyojung Lee [b,c], Francesco Calzaferri [a,2], Marco De Amici [a], Clelia Dallanoce [a], Pau Gorostiza [b,c,f,*], Carlo Matera [a,b,c,**]

[a] Department of Pharmaceutical Sciences, University of Milan, Milan 20133, Italy
[b] Institute for Bioengineering of Catalonia (IBEC), Barcelona Institute of Science and Technology, Barcelona 08028, Spain
[c] Networking Biomedical Center in Bioengineering, Biomaterials, and Nanomedicine (CIBER-BBN), ISCIII, Madrid 28029, Spain
[d] University of Barcelona—Doctoral program, Barcelona 08007, Spain
[e] Department of Pathology and Experimental Therapeutics, Faculty of Medicine and Health Sciences-Campus Bellvitge, University of Barcelona, Barcelona, Spain
[f] Catalan Institution for Research and Advanced Studies (ICREA), Barcelona 08010, Spain

ARTICLE INFO

Keywords:
Photopharmacology
Nicotinic Acetylcholine Receptor
Photoswitchable Ligand
Two-Photon Activation
Two-Photon Pharmacology
Zebrafish Behavioral Assay

ABSTRACT

The α7 nicotinic acetylcholine receptor (α7 nAChR) is a key modulator of neuronal and immunological signaling, and photopharmacology offers a route to control nicotinic transmission with high spatiotemporal precision. Here we report CPZ-2, a photoswitchable ligand inspired by a patented α7-active scaffold. CPZ-2 shows slow thermal relaxation, high photostability, and reversible photoswitching under one-photon irradiation, together with two-photon-induced photoisomerization monitored directly by HPLC–MS. Radioligand-binding competition performed on the trans-enriched state showed measurable displacement at α7 nAChRs and α1-containing receptors at 10 μM, with lower effects at α3β4 and α4β2 subtypes. Moreover, in wild-type zebrafish larvae, CPZ-2 modulated nicotine-evoked locomotion in a light-dependent manner after bath application. Finally, docking simulations in the α7 orthosteric site support a binding mode compatible with receptor engagement and suggest photostate-dependent differences in the orientation of the distal aromatic group relative to the C-loop region. Together, these data identify CPZ-2 as an uncharged, diffusible photoswitchable nicotinic ligand that combines robust one- and two-photon photochemistry with light-dependent modulation of nicotinic signaling in a wild-type vertebrate model.

1. Introduction

Nicotinic acetylcholine receptors (nAChRs) are ligand-gated ion channels that mediate fast synaptic transmission in the nervous system and are main actors in vital physiological processes, such as cognition, muscle contraction, and autonomic responses. They are widely distributed in the central and the peripheral nervous system [1], in the immune system, and in several peripheral tissues. The muscle-type nAChR is localized postsynaptically at the neuromuscular junction, where it is a key mediator of the electrical transmission creating the skeletal muscle tone. The numerous neuronal nAChR subtypes are located pre- and post-synaptically in autonomic ganglia and in cholinergic neurons throughout the central nervous system (CNS), where they are involved in a number of processes connected to cognitive functions, learning and memory, arousal, reward, motor control, and analgesia. The predominant subtypes functionally expressed in the brain are categorized as α7 subtype-containing receptors, or those composed of both α and β subunits, including the α4β2 and α3β4 subtypes [2]. Neuronal nAChRs are localized on the postsynaptic neuronal terminals or act as presynaptic receptors, thus indirectly modulating the release of various key neurotransmitters including dopamine, serotonin, GABA (γ-aminobutyric acid), glutamate, histamine, and norepinephrine [3,4].

* Corresponding author at: Institute for Bioengineering of Catalonia (IBEC), Barcelona Institute of Science and Technology, Barcelona 08028, Spain.
** Corresponding author at: Department of Pharmaceutical Sciences, University of Milan, Milan 20133, Italy.
E-mail addresses: pau@icrea.cat (P. Gorostiza), carlo.matera@unimi.it (C. Matera).
[1] Present address: Forschungzentrum Jülich
[2] Present address: Institut des Biomolécules Max Mousseron (IBMM), UMR 5247, CNRS-Université de Montpellier-ENSCM, 34296 Montpellier, France

https://doi.org/10.1016/j.biopha.2026.119727
Received 3 March 2026; Received in revised form 24 June 2026; Accepted 29 June 2026
Available online 3 July 2026

The homopentameric α7 nAChR is particularly intriguing for researchers as it is expressed on a variety of cell types in the periphery, including immune cells and neurons, as well as in brain regions that underlie learning and memory. In the CNS, α7 nAChRs are expressed on both neurons and non-neuronal cells, including astrocytes, microglia, oligodendrocytes precursor cells, endothelial cells, and chondroitin sulfate proteoglycan NG2-expressing cells, suggesting a possible role in brain innate immunity, inflammation, and neuroprotection. Functionally, α7 nAChRs can be distinguished from α4β2-containing receptors due to their unique physiological and pharmacological properties. In mammals, α7 nAChRs appear to be predominantly homomeric ion channels with five potential ligand-binding domains (*LBDs*) hosted and located at the interface between two alpha subunits. In addition to these orthosteric binding sites, the α7 nAChR subtype hosts multiple allosteric sites [5], structurally distinct from the orthosteric one and bound by the allosteric modulators. α7 nAChRs are characterized by low affinity for acetylcholine (ACh), but they are blocked by nanomolar concentrations of the snake toxin α-BTX (α-bungarotoxin) and show a high relative permeability to calcium. Therefore, α7 nAChRs play a role also in direct activation of calcium-dependent processes, such as interneuron excitability, release of excitatory and inhibitory neurotransmitters, and neuroprotection. Overall, the α7 nAChR is broadly diffused and involved in several physiological and pathological processes, making it an attractive therapeutic target for Alzheimer's disease, Parkinson's disease, neurodevelopmental disorders, schizophrenia, attention-deficit/hyperactivity disorder (ADHD), and low-functioning autism, among others [6–9]. Another emerging research field explores the development of anti-inflammatory therapies aimed at the α7 receptor [10–12].

The ubiquitous expression of the receptor underlines its importance but implies an equally high probability of off-target interactions and potential adverse effects. Therefore, the possibility to precisely control its activity in a spatiotemporal manner is highly appealing and has been the focus of numerous research efforts. In this context, photopharmacology emerges as an excellent strategy, with the potential to address these challenges. The photopharmacological approach has already proven successful in the control of the nicotinic transmission. In the late 1960s, Erlanger and Nachmansohn demonstrated that the photochromic ligands p-phenylazophenyltrimethylammonium (azo-PTA) and N-p-phenylazophenyl-N-phenylcarbamylcholine (azo-Ph-carbachol) were photoswitchable inhibitors of acetylcholine receptors. Both compounds were found to function as antagonists in their *trans* form in electroplax membranes, while *trans* to *cis* isomerization under 320 nm UV light resulted in a large depolarization in the presence of the agonist carbachol [13]. Shortly after, Erlanger and Wassermann presented the photochromic nAChR agonist BisQ, that can be considered an azologue of the known nAChR partial agonist decamethonium, where the carbon chain is replaced by an azobenzene moiety. The *trans* isomer of BisQ was found to be a very potent nAChR agonist, inducing depolarization of the electroplax membrane. Rapid repolarization of the membrane then occurred when irradiating with 360 nm light [14]. In 1969, Silman and Karlin introduced the idea of covalently tethering an agonist to a nAChR: they presented QBr, a BisQ derivative in which a bromine atom replaces one of the trimethylammonium groups. This modification converted the freely diffusible ligand into a covalent ligand [15]. In 2012, Trauner and Kramer introduced the genetically engineered light-controlled nAChR (LinAChR). They rationally designed two covalent photoswitchable nicotinic ligands, the agonist MAACh and the antagonist MAHoCh. The engineered α3β4 and the α4β2 nAChRs, expressed in *Xenopus laevis* oocytes, were both turned into photoreceptors when the agonist MAACh was used. Furthermore, light induced inhibition of nAChR current was achieved by attaching the antagonist MAHoCh to the same cysteine residue in α3β4 and α4β2 nAChRs [16]. The latest addition to the cholinergic photopharmacology toolbox was the photochromic ligand AzoCholine [17]. This compound can be isomerized between its *cis* and *trans* configurations by illumination with 360 nm and 440 nm light, respectively. AzoCholine proved to be a photoswitchable *trans*-active agonist in patch-clamp electrophysiology recordings in an α7 nAChR/glycine receptor chimera that was heterologously expressed in HEK 293 T cells. AzoCholine was also tested on mouse hippocampal brain slices: in the presence of the photochromic agonist, the neuronal activity could be modulated by toggling between 360 and 460 nm, in agreement with results obtained in HEK cells. However, its activity was not evaluated across different nAChR subtypes, and activation with longer wavelengths was not reported. Finally, experiments in the invertebrate *Caenorhabditis elegans* demonstrated that this photoswitch can perturb its swimming behavior in a light-dependent manner, although some results were unclear and warrant further investigation. Another limitation of AzoCholine is its permanent charge, which restricts blood–brain barrier permeability and limits its potential use as a CNS photomodulator.

To our knowledge, no diffusible photoswitchable ligand targeting native α7 nAChRs has yet been demonstrated to function (centrally) in vertebrates. This represents a major obstacle to study the physiological role and mechanism of such a ubiquitous and important target. To address these limitations, we aimed to develop a photoswitchable α7 nAChR ligand that combines key properties not available in previous tools, such as preference among neuronal nAChR subtypes, an uncharged and potentially brain-permeant scaffold, photoisomerization with tissue-penetrating light, and demonstrated applicability in live wildtype vertebrates. Drawing on our experience in nicotinic ligand design, we conceived our ideal target compound with these objectives in mind [18–21], and here we present its chemical synthesis, photochemical characterization, and photopharmacological properties in vitro and in vivo.

2. Design & synthesis

The aim of our molecular design was to combine excellent photochemical and pharmacological properties in a single compound. During the last decade, many bioactive small molecules have been converted into photoswitchable ligands by "azologization", a rational strategy to design based on replacing certain core motives with a bioisosteric photoisomerizable diarylazo moiety [22]. This approach preserves the structural framework of the original compound, generally with minimal disruption of its pharmacological and physicochemical properties. To identify a molecular scaffold that retained these valuable properties while allowing the engineering of its photochemical profile, we searched for suitable α7 ligands in the literature, including patents. At the end of this survey, we selected as parent compound for our work a patented α7 ligand [23], indicated as *example 49* in the patent and named as compound **A** in the present article (Fig. 1). In WO2007138033A1, members of this 2-phenyl−5-amino−1,3,4-oxadiazole series were characterized using an α7 nAChR FLIPR assay that reports pEC_{50} values ($pEC_{50} \geq 5$ for compound **A**), suggesting that the patented compounds were evaluated primarily in agonist mode (agonists/partial agonists), although detailed efficacy and mechanism are not consistently disclosed for individual examples. Accordingly, we did not assume an agonist mode of action upon photoswitch incorporation. Beyond having a structure amenable to azologization, an uncommon characteristic among α7 ligands, the information reported in the patent by Coppo and co-inventors and subsequent patents suggests that the change in the relative position of the two aromatic rings in this kind of ligands is critical [24,25]. This supports the expectation that azobenzene analogs ("azologs") of the parent scaffold may display photostate-dependent pharmacology (i.e., different activity of the *trans* and *cis* isomers), a key prerequisite for effective photopharmacology. Such functional "photoswitchability" cannot be assumed a priori, as the geometric change introduced by the arylazo unit does not necessarily translate into measurable differences in receptor activity.

On this basis, three putative photoswitchable α7 ligands, named **CPZ−1**, **CPZ−2**, and **CPZ−3**, were designed (Fig. 1). **CPZ−1** was devised via direct azologization by replacing the amide bridge between

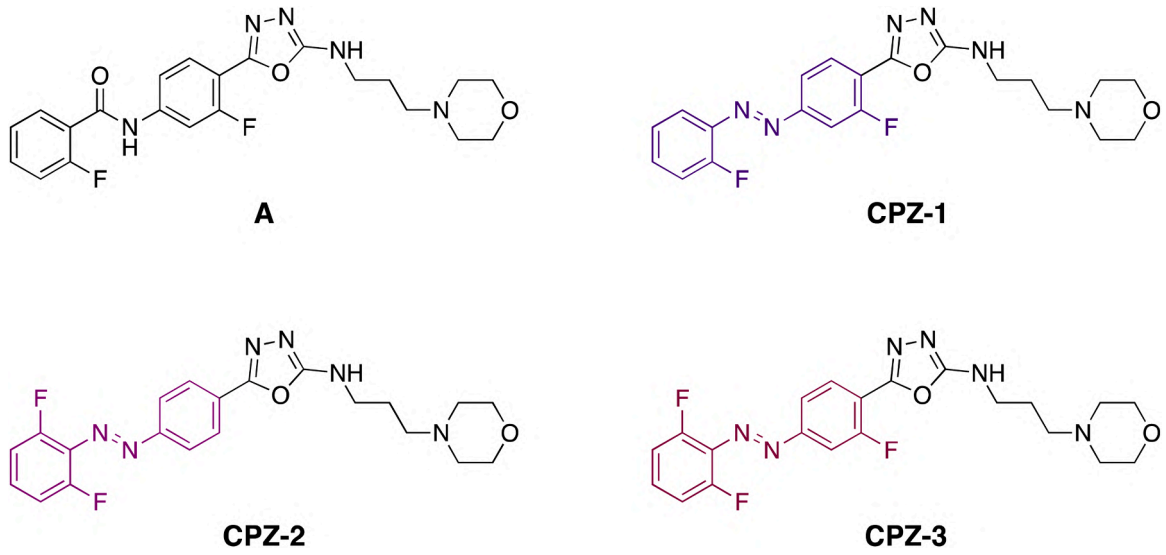

Fig. 1. Chemical structures of the parent α7 nAChR ligand (compound A, indicated as *example 49* in the patent) [23] and the designed azologs.

the two aromatic rings with an azo group. **CPZ—2** was specifically designed to enhance the efficacy of isomerization with infrared (IR) light by means of two-photon excitation (2PE). Indeed, a crucial aspect that should be addressed to unleash the full potential of azobenzene-based photoswitches is multiphoton excitation with IR light, which enables high penetration and sub-micrometric resolution in three dimensions [26–32]. As recently conceived and rationalized by Cabré et al., [33] an effective approach to obtain azobenzene-based photoswitches with high 2PE for biological applications involves designing electronically asymmetric azoaromatic photochromes that feature weak mesomeric electron-donating groups (EDGs) and electron-withdrawing groups (EWGs) combined with strong inductive EWGs. With these principles in mind, in **CPZ—2** the 2-amino−1,3,4-oxadiazole moiety of the parent compound was maintained to provide a weak donor component in *para* position with respect to the azo bridge on the middle phenyl ring, while fluorine substitution was introduced at the unsubstituted *ortho* position of the terminal phenyl ring to provide a strong inductive electron-withdrawing component and increase electronic asymmetry. Lastly, **CPZ—3** was designed to investigate the effects of a different substitution pattern in the aromatic region on the photochemical and photopharmacological properties. Specifically, in comparison to **CPZ—1**, an additional fluorine atom was introduced in the ortho position (with respect to the azo bridge) on the terminal phenyl ring of **CPZ—3**.

The three azologs, **CPZ—1**, **CPZ—2**, and **CPZ—3**, share similar synthetic steps. The general route, loosely inspired by the one reported for the parent compound **A**, is depicted in Scheme 1. The para-nitrobenzoic acid derivatives (**1 h**, **1 f**) were first converted into the hydrazide derivatives (**3 h**, **3 f**) in a two-step process via the methyl ester intermediates (**2 h**, **2 f**) to ensure efficient conversion. Subsequently, these hydrazides were transformed into the corresponding 2-mercapto−1,3,4-oxadiazoles (**4 h**, **4 f**) through a well-known procedure in presence of CS_2. The thiol intermediate was afterwards reacted with benzyl bromide to provide the benzyl mercaptan intermediates (**5 h**, **5 f**), that were then oxidized with $KMnO_4$ to afford the corresponding sulfone derivatives (**6 h**, **6 f**). The so-obtained benzenesulphonyl leaving group was in turn substituted by a *N*-(3-aminopropyl)morpholine (**7 h**, **7 f**). Catalytic hydrogenation of the nitro group afforded the advanced amine derivatives (**8 h**, **8 f**). Due to the high susceptibility of these intermediates to unwanted oxidation, all subsequent reactions and manipulations were conducted under an inert atmosphere whenever feasible. The 1-fluoro- (**10 h**) and 1,2-difluoro- (**10 f**) nitrosobenzene intermediates were prepared by oxidizing the corresponding amines (**9 h**, **9 f**) with Oxone® in a biphasic dichloromethane-water system. The advanced aniline intermediates (**8**) and the nitroso compounds (**10**) were finally condensed via a modified Baeyer-Mills reaction in a 6:6:1 mixture of acetic acid, trifluoroacetic acid, and toluene. Disappointingly, HPLC-MS analyses revealed that **CPZ—1** and **CPZ—3** were obtained as the corresponding azoxybenzenes instead of the expected azobenzenes (Figure S1). Azoxybenzenes are undesired side-products of the Baeyer-Mills reaction, the formation of which can considerably decrease the reaction yields. They generally derive from the coupling of phenylhydroxylamines (produced in situ from phenylamines in a side reaction) and nitrosobenzenes. We hypothesize that our nitroso compounds might easily oxidize the common aniline intermediate used for the preparation of **CPZ—1** and **CPZ—3** to give the corresponding phenylhydroxylamine, which could ultimately condense with the remaining nitrosobenzenes to produce azoxybenzenes. In contrast, **CPZ—2** was successfully obtained as intended and underwent a more comprehensive analytical characterization (see also Figures S2–S5). Remarkably, all three compounds displayed good aqueous solubility (0.5% DMSO).

3. Photophysical & photochemical characterization

The photochemical behaviour of our final compounds was studied by UV-VIS spectroscopy and HPLC-MS. Azoxy-**CPZ—1** and azoxy-**CPZ—3** showed suboptimal photochemical properties, even undergoing an irreversible reaction upon irradiation at 365 nm, likely a photo-Wallach rearrangement [34], which made them unsuitable for our purposes. Consequently, these compounds were ruled out for further development and omitted from subsequent experimental evaluations.

CPZ—2 was initially characterized by standard UV-Vis spectroscopy. The molecule exhibited a prominent π-π* absorption band centered around 350 nm and a weaker n-π* absorption band at approximately 440 nm in aqueous solution (0.5% DMSO, 50 μM). Irradiation with 380 nm light gave maximal *trans*-to-*cis* isomerization, while the reverse *cis*-to-*trans* isomerization was efficiently achieved using light at 430 nm, demonstrating its capacity to photoisomerize reversibly. Interestingly, irradiation at 500 nm led to a photostationary state apparently closer to the *cis* form, as confirmed later (Fig. 2**A**). HPLC-MS chromatograms for **CPZ—2** revealed a maximum conversion of 67% to the *cis* isomer at 380 nm and 64% to the *trans* isomer at 430 nm, while illumination at 500 nm yielded a *cis/trans* ratio of about 55/45 (Fig. 2**B**). Although the conversions at 380 and 430 nm are, as noted, not quantitative, the ability of the compound to effectively photocontrol its target depends on the relative biological activity of the isomers, which must be determined

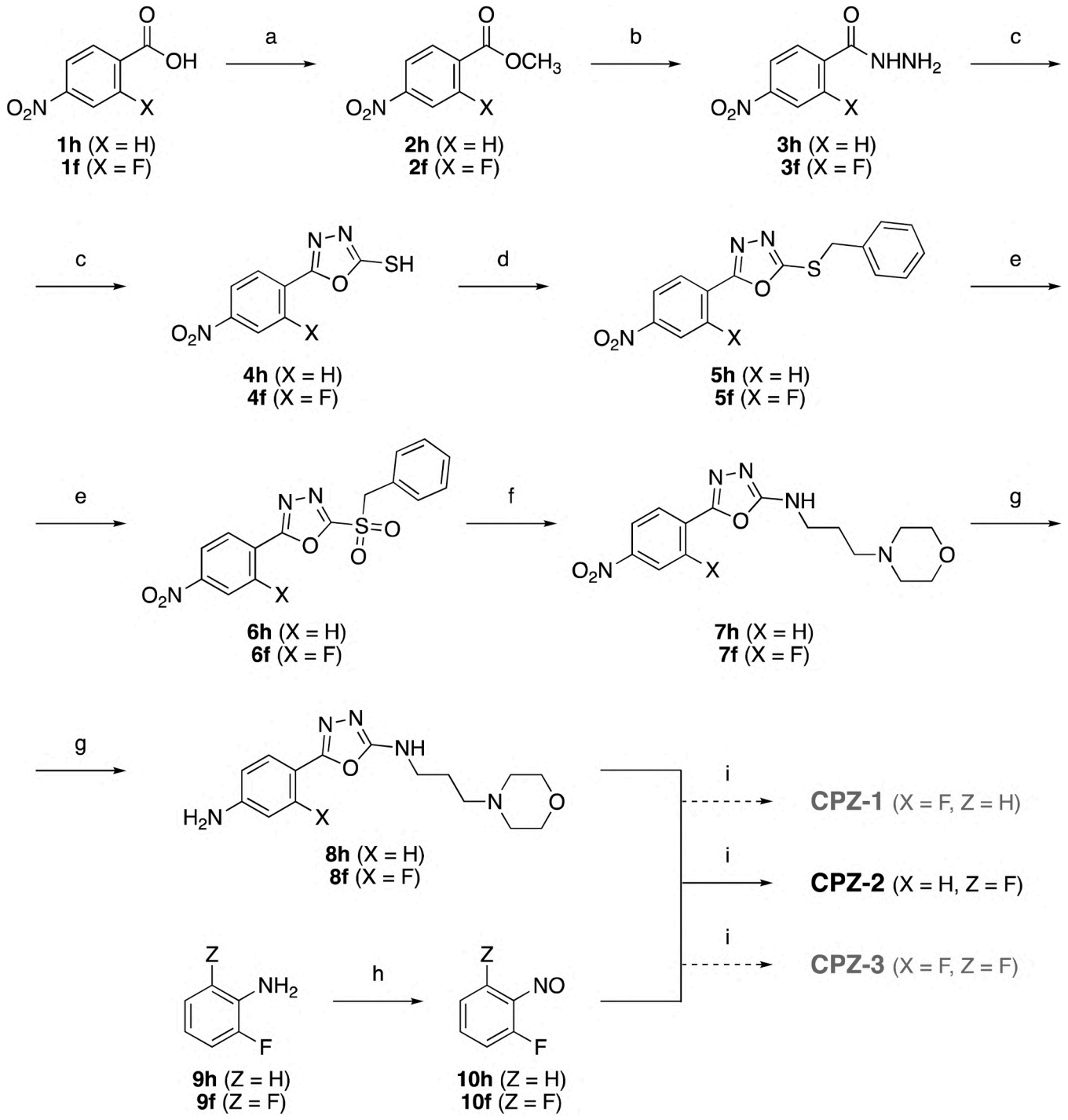

Scheme 1. Synthetic pathway to compounds CPZ−1, CPZ−2, and CPZ−3. (a) MeOH, H_2SO_4, 75 °C, overnight; (b) $NH_2NH_2H_2O$ in MeOH, 0 °C, 30 min → 60 °C, 6 h; (c) CS_2, Et_3N in EtOH, overnight; (d) BnBr, in DMF, 2 h; (e) $KMnO_4$, AcOH, 15 min, 10 °C; (f) *N*-(3-aminopropyl)morpholine, dioxane, RT, instantaneous; (g) H_2 1 atm, Pd-C 10%, EtOH, RT, overnight; (h) Oxone®, DCM/H_2O, under inert atmosphere, RT, 24 h; (i) TFA:AcOH:toluene 6:6:1, under inert atmosphere, overnight, RT. CPZ−1 and CPZ−3 were not obtained, only the corresponding azoxybenzenes were isolated.

empirically. Regarding the kinetics of thermal relaxation, the *cis* isomer exhibited remarkable stability when kept in the dark, showing no significant changes in absorbance over 180 min (Fig. 2**C**), in agreement with the photochemical design [33]. Furthermore, the molecule displayed excellent photostability, with no evidence of photobleaching or degradation during multiple photoisomerization cycles across the most relevant wavelengths (Fig. 2**D**).

As previously described, **CPZ−2** was rationally designed as a molecular system capable of undergoing switching by 2PE. For this purpose, we devised a macroscopic assay to investigate this property using widely available chemical characterization tools and a pulsed laser light source that can be found in shared photochemical and biological imaging facilities. Since effective 2PE is only attained at the focal point of the laser (generally corresponding to a volume of ~10 μL), a 200 μL volume of a 50 μM solution of **CPZ−2** was irradiated using the laser source of a two-photon laser scanning microscope operating at 760 nm. At regular intervals of 30 min, 3 μL aliquots of the irradiated solution were taken and subsequently analyzed by HPLC-MS for precise

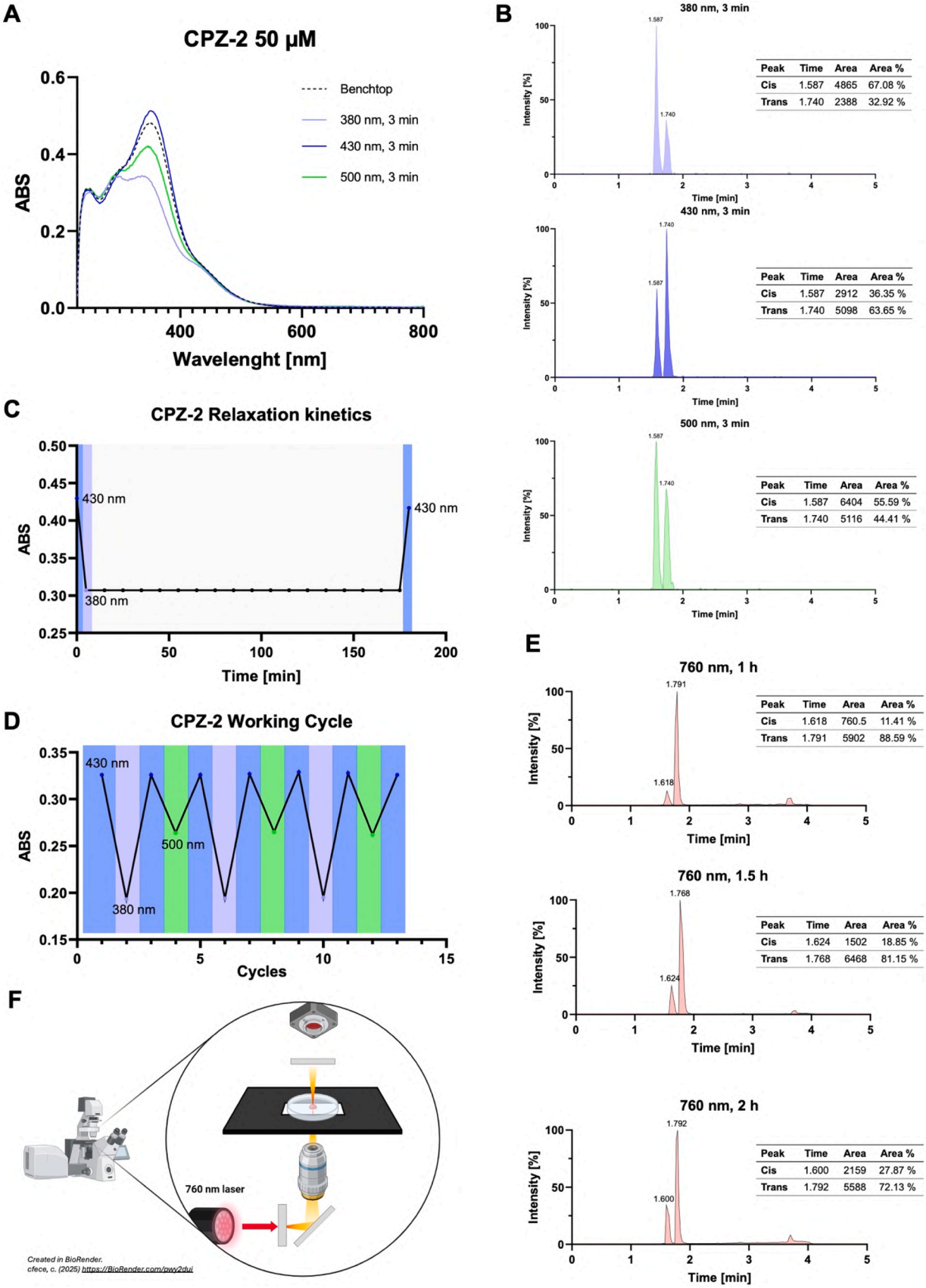

(caption on next page)

Fig. 2. Photochemical characterization of CPZ−2. (A) UV-Vis absorption spectra of CPZ−2 in aqueous solution (0.5% DMSO, 50 μM) showing a π-π* absorption band at ~350 nm and an n-π* band at ~440 nm. Maximal *trans*-to-*cis* isomerization was achieved at 380 nm, while reverse *cis*-to-*trans* isomerization occurred at 430 nm. Irradiation at 500 nm resulted in a photostationary state favoring the *cis* isomer. (B) HPLC-MS chromatograms of CPZ−2 revealing isomerization efficiency: 67% *cis* at 380 nm, 64% *trans* at 430 nm, and a *cis/trans* ratio of ~55/45 at 500 nm. (C) Thermal relaxation kinetics of the *cis* isomer in the dark, demonstrating remarkable stability over 180 min. (D) Photostability of CPZ−2 under multiple photoisomerization cycles, with no photobleaching or degradation detected. (E, F) Two-photon switching behavior of CPZ−2 using a bulk chemical assay and a facility 2PE microscope. A 200 μL drop of a 50 μM CPZ−2 solution was irradiated in fast raster scan in the X and Y direction for all the field of view of the microscope with a pulsed laser (760 nm, 1 mW mean power), and aliquots were analyzed by SIR-HPLC-MS at 30-min intervals, showing a progressive increase in the *cis/trans* isomer ratio, confirming photoinduced switching under the experimental conditions used. Panel F was created in BioRender. cfece, c. (2025) https://BioRender.com/pwy2dui.

monitoring of the photoconversion process over time. Consistent with our expectations, the analysis revealed a clear and progressive increase in the *cis/trans* isomer ratio, providing direct evidence of the photoinduced switching behavior of the molecule under the experimental conditions (Fig. 2**E,F**). Here, two-photon switching is demonstrated in bulk solution as a photochemical enabling property, while spatially confined receptor modulation in tissue was not examined in this work. Notably, this HPLC–MS-based readout provides a simple and accessible way to assess bulk two-photon-induced photoisomerization of molecular photoswitches without relying on biological reporters or fluorescence-based activity assays.

4. Biological evaluation

We then assessed receptor engagement in a radioligand-binding competition panel outsourced to a third-party facility. Due to logistical constraints and the inability to perform photoisomerization in situ, only the *trans*-enriched state was tested. Accordingly, these data do not allow a *cis/trans* comparison in radioligand displacement. At 10 μM, **CPZ−2** produced radioligand displacement at α7 (25%) and α1-containing receptors (22%), with lower inhibition at α3β4 (12%) and α4β2 (5%) subtypes (Figure S6). These data are consistent with target engagement of nicotinic receptors by the *trans*-enriched state and provide converging evidence supporting receptor interaction.

Following the photochemical and in vitro characterization of **CPZ−2**, we finally evaluated its ability to modulate nicotine-evoked locomotion in zebrafish larvae as a function of concentration and photostate (Fig. 3). Zebrafish have emerged as a tractable vertebrate model to quantify nicotine-driven behavioral phenotypes and their underlying molecular adaptations. In adult zebrafish, nicotine-induced conditioned place preference and reward-related behaviors are shaped by epigenetic regulation, including histone methylation and DNA methylation pathways, and these processes are accompanied by changes in the expression and promoter methylation of nicotinic receptor subunits such as α7 [35,36]. Moreover, nicotine exposure and subsequent withdrawal can produce long-lasting changes in reward sensitivity and brain gene expression, further supporting zebrafish as a relevant system to probe nicotinic neuroadaptations [37]. Zebrafish larvae (48 h post fertilization, hpf) provide a convenient and biologically meaningful system for our purpose because they readily absorb small molecules from the surrounding water and display robust, quantifiable locomotor responses to nicotine [38]. Moreover, larvae can be assayed in multi-well plates in a high-throughput format that we and others have previously used for photopharmacological studies [38]. To probe photostate-dependent effects in vivo, we tested **CPZ−2** at 5 μM and 10 μM and generated the corresponding photostationary states (PSS) by pre-illuminating the dosing solutions for 5 min at 365 nm (*cis*-enriched) or 455 nm (*trans*-enriched). This duration exceeds the 3 min used to generate the PSS chromatograms (Fig. 2**B**), and the corresponding compositions are best approximated by the HPLC–MS values measured at the nearest characterized switching wavelengths (67% *cis* at 380 nm and 64% *trans* at 430 nm; Fig. 2**B**).

Incubation of larvae with CPZ−2 alone in either photostate (Fig. 3c,f; locomotion time course and quantification, respectively) did not significantly alter swimming activity relative to control. This suggested that any behavioral effects were more likely to emerge in the presence of a cholinergic stimulus. We therefore used nicotine, which reliably increases larval locomotion, as a sensitized behavioral readout to detect modulation by CPZ−2 [38]. When CPZ−2 was co-administered (5 or 10 μM) with 60 μM nicotine (Fig. 3d,g), the *cis*-enriched condition significantly reduced nicotine-evoked locomotion relative to nicotine alone, whereas the *trans*-enriched condition produced a smaller or non-significant effect in the same assay. At higher nicotine concentration (120 μM; Fig. 3e,h), differences between conditions were smaller and more variable, and the apparent direction and magnitude of modulation were more sensitive to baseline activity and the choice of analysis window. Importantly, the in vivo phenotype should not be over-interpreted as a direct reflection of α7 pharmacology alone, because the direction and magnitude of behavioral modulation likely reflect integrated contributions from multiple nicotinic receptor populations, together with differences in effective exposure, tissue distribution, and PSS composition in vivo. Nonetheless, these experiments demonstrate that CPZ−2 reaches relevant sites after simple bath application and can modulate nicotine-evoked behavior in a light-dependent manner.

The robust increase in locomotor activity observed in nicotine-treated larvae is consistent with previous behavioral studies, supporting the validity of our assay. Nicotine exposure at embryonic and early larval stages has been reported to elevate locomotion with a comparable magnitude and time course, in a dose-dependent manner [38,39]. To enable direct comparisons across conditions, we quantified **CPZ−2** effects within a predefined analysis window aligned with nicotine administration, providing a standardized basis for assessing photostate-dependent modulation. Zebrafish at this developmental stage express several nAChR subtypes in key regions that regulate movement, including α7, heteromeric receptors such as α4β2-related subtypes, and α1-containing receptors at the neuromuscular junction [39–43]. The selective α7 antagonist methyllycaconitine (MLA) has been reported to attenuate nicotine-driven phenotypes at early larval stages [41], supporting a role for α7 signaling in this model, while heteromeric nAChRs have also been implicated in CNS-driven behavioral effects. At the same time, we cannot exclude contributions from α1-containing receptors, which are abundant at larval neuromuscular junctions, and for which our binding data indicate measurable engagement by **CPZ−2** in the *trans*-enriched state (Figure S6).

Overall, our behavioral results establish that **CPZ−2** enables light-dependent modulation of nicotine-evoked locomotion in zebrafish larvae, consistent with engagement of nicotinic signaling in vivo. Given the diversity of nicotinic receptor subtypes expressed at this developmental stage and across neuromuscular and CNS compartments, the observed phenotype likely reflects contributions from more than one nAChR population. Finally, the demonstrated two-photon photoswitching of **CPZ−2** in bulk solution supports its compatibility with standard two-photon optical setups as an enabling photochemical feature.

5. Computational studies

The α7 nAChR displays fast conformational dynamics and substantial structural rearrangements during gating, resulting in a binding pocket whose shape and accessibility are strongly influenced by motions of the C loop. This conformational plasticity has historically complicated

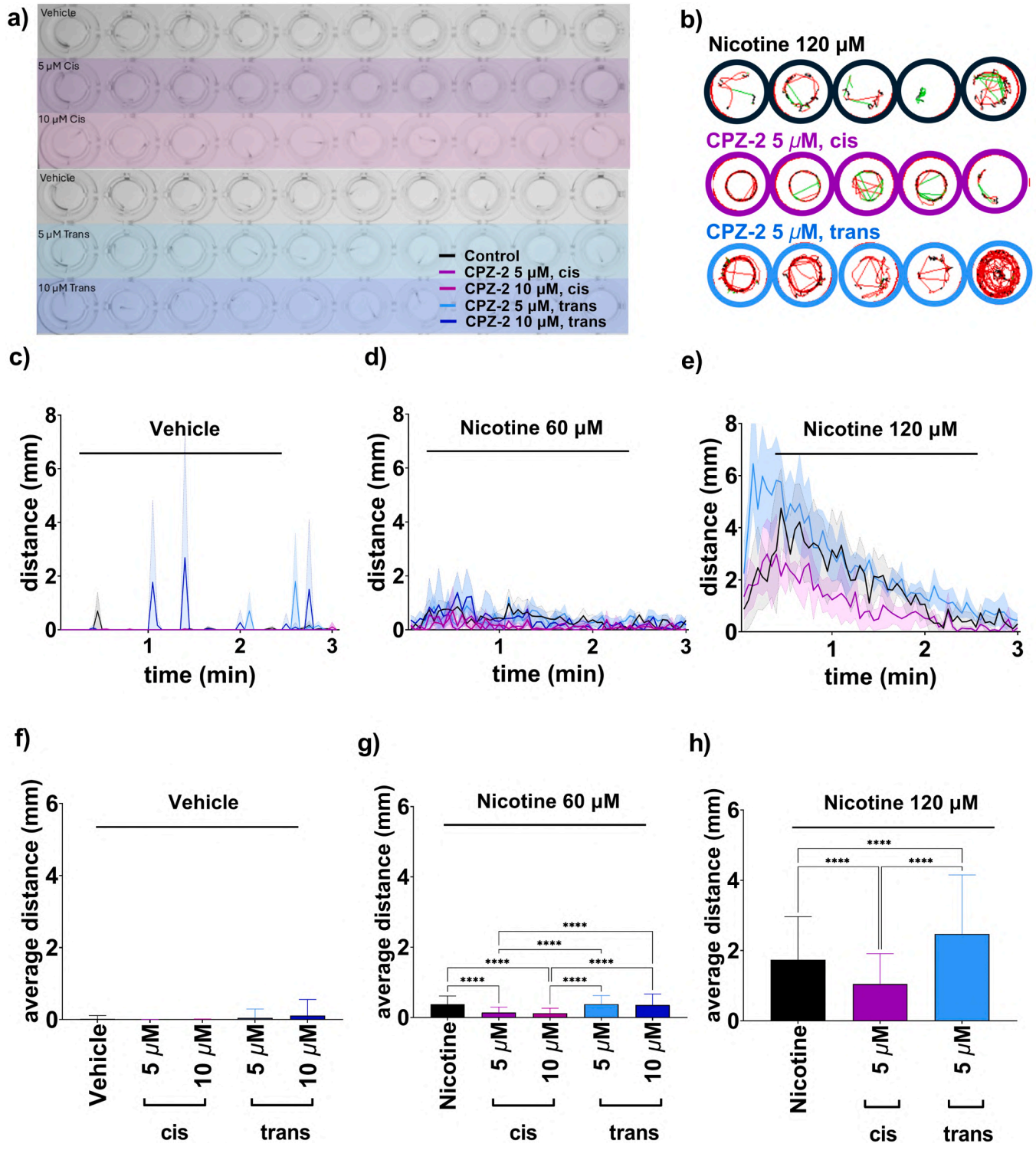

Fig. 3. Locomotor responses of zebrafish larvae at 48 hpf. a) Description of the larval arrangement for the experiment in 96-well plates. b) Example of the recording of 5 fish with 120 µM of nicotine and CPZ−2. Fast (red) and slow (green) movements recorded with the Zebrabox (ViewPoint) were classified following the procedure described in our previous work [44]. c), f) Treatment of zebrafish larvae using *cis* and *trans* CPZ−2. d), g) Treatment of zebrafish larvae using 60 µM nicotine, alone and in combination with *cis* or *trans* CPZ−2. e), h) Treatment of zebrafish larvae using 120 µM nicotine, alone and in combination with *cis* or *trans* CPZ−2. Time course graph representing the mean distance traveled plotted against time. The shaded areas represent standard error of the mean (SEM). For the bars graph, data were analyzed using two-way ANOVA followed by Tukey's post-hoc test. Data represent the mean ± SD. * $p \leq 0.05$; ** $p \leq 0.01$; *** $p \leq 0.001$; **** $p \leq 0.0001$; For all conditions, n = 10 larvae.

structure-based inference and crystallographic efforts, and high-resolution structural information has only recently become available through cryo-EM, which provides an improved framework to rationalize ligand–receptor interactions in native-like architectures [45,46]. On this basis, and to obtain qualitative insights into how photoisomerization might influence receptor engagement, we performed docking simulations of **CPZ−2** in its *trans* and *cis* geometries.

The predicted docking scores showed a small but clear preference for the *trans* isomer (Tables S1–S2). Interestingly, the best scoring poses suggested differences in the orientation of the azo-containing aromatic system within the binding cavity (Fig. 4**A,B**). In both cases, the aliphatic chain, the oxadiazole moiety, and the proximal aromatic ring occupied similar regions of the pocket, consistent with a conserved anchoring mode. The protonatable morpholine nitrogen adopted different orientations in the two isomers, but in both cases remained compatible with a predominantly intramolecular cation–π interaction, as reported for α7 ligands [45], while the oxadiazole scaffold engaged polar contacts (including a hydrogen bond with Trp148) and the proximal aromatic region established π–π/π–sulfur and hydrophobic interactions with residues lining the aromatic box (e.g., Tyr187, Tyr194, Cys189). The main qualitative divergence concerned the placement of the terminal difluorinated phenyl ring: in the *cis* isomer, this group preferentially adopted an orientation projecting toward the region proximal to the C-loop trajectory (Fig. 4**A**), whereas in the *trans* isomer it more often aligned along the C-loop surface and engaged alternative hydrophobic contacts (Fig. 4**B**).

Taken together, these results support a binding mode for **CPZ−2** compatible with orthosteric-site engagement at α7 nAChRs and suggest a plausible structural basis for photostate-dependent receptor interaction. In particular, differences in how the terminal aromatic group occupies space near the C-loop may translate into distinct steric and interaction patterns within a region that is central to receptor gating. While these docking models do not define the functional mode of action of CPZ−2, they provide a qualitative structural rationale for why *cis*- and *trans*-enriched photostates may interact differently with α7-related binding sites [47].

6. Conclusions

In conclusion, **CPZ−2** behaves as a photoswitchable nicotinic ligand that combines a robust photochemical profile with measurable engagement of nAChR binding sites, including α7 nAChRs. It displays reversible trans–cis photoisomerization, slow thermal relaxation, excellent photostability, and two-photon photoswitching in bulk experiments, supporting its compatibility with optical control strategies as an enabling photochemical feature. In addition, the HPLC–MS-based assay used here provides an accessible chemical readout to assess bulk two-photon-induced photoisomerization without relying on biological reporters or fluorescence-based functional assays. In vivo, **CPZ−2** modulates nicotine-evoked locomotion in wild-type zebrafish larvae in a

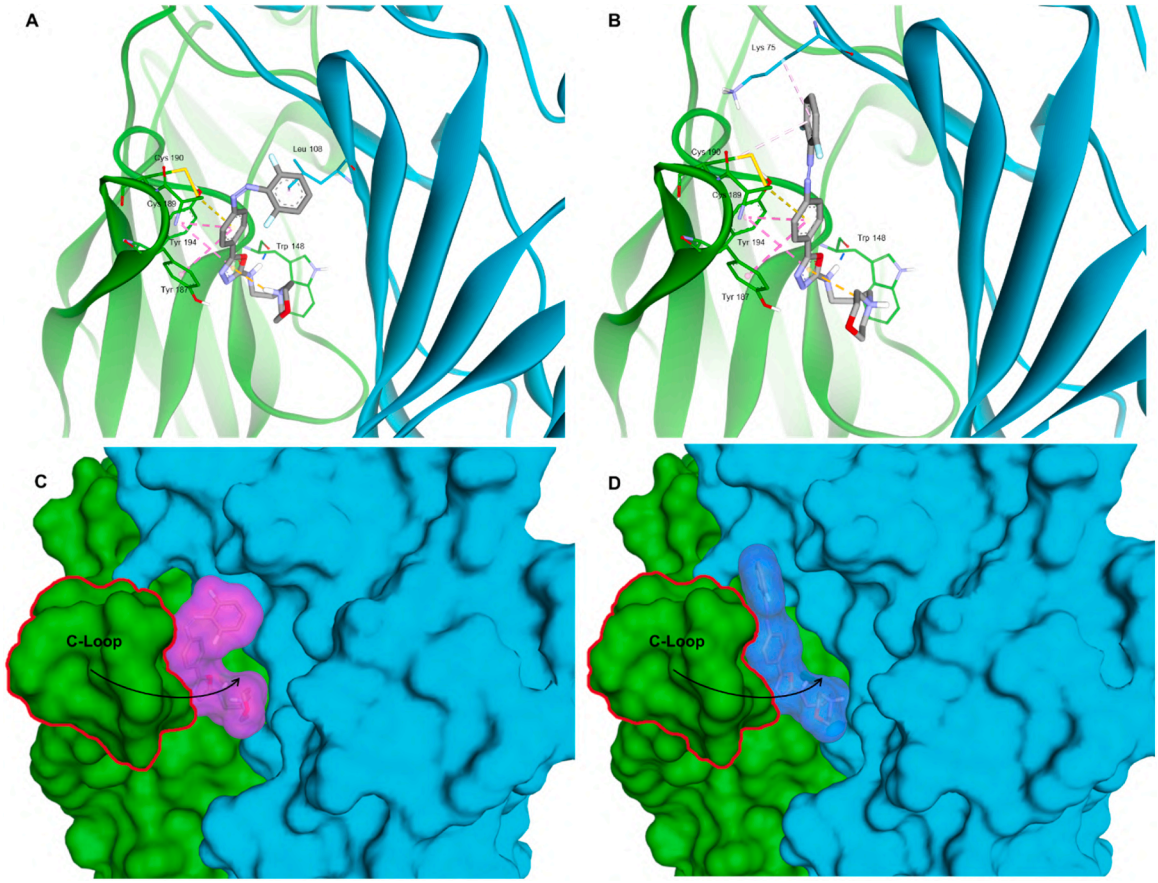

Fig. 4. Docking models of *cis*- and *trans*-CPZ−2 in the orthosteric binding site of the α7 nAChR extracellular domain (PDB ID: 7KOO). The binding site is located at the interface between the principal (+) subunit (green) and the complementary (–) subunit (cyan). Key binding-site residues are shown as sticks (colored by subunit). (A) Representative docked pose of *cis*-CPZ−2 highlighting predicted contacts with binding-site residues. (B) Representative docked pose of *trans*-CPZ−2 highlighting predicted contacts with binding-site residues. (C,D) Solvent-accessible surface representations for the *cis* (C) and *trans* (D) poses, illustrating relative pocket occupancy. The C-loop is highlighted in red to provide structural context (arrow indicates the reported direction of C-loop motion during gating). In the docking models, both isomers display broadly similar anchoring of the oxadiazole-containing core, whereas the distal difluorophenyl ring adopts distinct orientations, resulting in different steric proximity to the C-loop region. CPZ−2 is shown as sticks (carbon, gray; oxygen, red; nitrogen, blue; sulfur, yellow; polar hydrogens shown). Predicted noncovalent interactions (e.g., hydrogen bonds, π–π/π–cation, and hydrophobic contacts) are indicated by dashed lines.

light-dependent manner following simple bath application, demonstrating that the compound reaches relevant targets in an intact vertebrate preparation and can be used to perturb nicotinic signaling with temporal control. While the behavioral phenotype is consistent with engagement of nicotinic pathways, its circuit-level origin is expected to reflect contributions from multiple nAChR populations expressed in the larval neuromuscular system and CNS. Accordingly, **CPZ−2** provides a valuable entry point to explore light-dependent modulation of cholinergic function in vivo. Computational docking analyses support a binding mode compatible with orthosteric-site engagement at α7 nAChRs and suggest that photoisomerization can alter the spatial disposition of the distal aromatic group relative to the C-loop region, offering a qualitative structural rationale for photostate-dependent receptor interaction.

Taken together, these results expand the photopharmacology toolbox with a diffusible, uncharged, light-regulated nicotinic ligand that is compatible with one-photon and two-photon control, and is directly active in a wild-type vertebrate model. **CPZ−2** provides a practical starting point for mechanistic studies of nicotinic signaling in neurobiology and a platform for subsequent analog exploration.

7. Materials & methods

7.1. Chemicals, reagents and equipment for chemical synthesis and analysis

All commercial reagents were purchased from Sigma-Aldrich unless otherwise specified and they were used as received. Solvents for reactions were of analytical grade and used as received.

TLC silica gel and stains. Reactions were monitored by TLC analyses performed on commercial silica gel 60 F_{254} aluminium sheets (Merck). Spots were observed with UV-lamp (λ = 365 nm) and/or evidenced with different TLC stains.

Column chromatography. Column chromatography separations were performed on silica gel Baker (0.063–0.200 mm) as stationary phase; eluents have been specified time to time. All reagents and solvents for the reactions were of analytical grade and were used without further purification.

^{1}H and ^{13}C NMR. Spectra were recorded on a Varian Mercury−300 and a Varian Mercury−400 instruments (300/400 and 75.0/101 MHz, respectively). Chemical shifts (δ scale) are reported in parts-per-million (ppm) relative to the peak of the internal standard TMS (δ = 0.00 ppm) for $CDCl_3$, CD_3OD, $(CD_3)_2CO$ or relative to the central peak of the solvent (δ = 2.50 ppm for $(CD_3)_2SO$) in ^{1}H NMR spectra and relative to the central peak of the solvent (δ = 77.16 ppm for $CDCl_3$, 49.00 for CD_3OD, 39.52 for $(CD_3)_2SO$ (DMSO-d6), and 29.84 for $(CD_3)_2CO$) in ^{13}C NMR spectra. Processing of the spectra was performed with MestReNova 8.1.1. Coupling constants (*J*) are reported in hertz (Hz). For each compound analysed, the specific deuterated solvent used is reported.

HPLC-PDA-MS. HPLC-PDA-MS chromatograms were registered using a Waters Alliance 2795 separation system, coupled with a Waters 996 photodiode detector (PDA) (210–800 nm) and a Waters 3100 Mass Detector (single quadrupole; electrospray ionization) with the MassLynx software for data acquisition. The separation module was equipped with a XSelect C18 4.6x50mm 3.5 μm column, the injection volume was set to 15 μl. The mobile phases were water (with 0.1% formic acid) as solvent A and acetonitrile (with 0.1% formic acid) as solvent B. The flow rate was set to 1.6 ml, and the elution program, run over 5 min, was as follows: 0.00 min: A= 95%, B= 5%; 3.50 min: A= 0%, B= 100%; 4.50 min: A= 95%, B= 5%; 5.00 min: A= 95%, B= 5%. The raw files were then elaborated using OpenChrom 42 in order to extract the XIC or SIR spectra (m/z: 429.0 ± 0.2) [48]. The peak area was calculated using the "Area Under the Curve" function in GraphPad Prism 8.

7.2. Optical equipment, methods and protocols

Illumination equipment. The illumination of the samples for the one-photon conversion was conducted with custom made LED plates, bearing LEDs of two different wavelengths. The selection of the wavelength was controlled via a Control Unit of Light. The light intensity emitted by the plate was fixed, at 0.5 mW·cm^{-2}. The illumination for the two-photon conversion was conducted with the use of a two-photon confocal microscope, bearing a Mai Tai Ti:Sapphire pulsed laser. The output power was controlled via a computer, and set at 1 mW, concentrated at the focal point.

Illumination protocols. To achieve photoconversion, 1 ml of the solution in a quartz cuvette was irradiated in a closed reflective box for 3 min, using the led plate at the chosen wavelength. To determine the qualitative conversion of the compound, the cuvette was then put in the UV-vis spectrometer trying to avoid light exposure. To determine quantitative conversion the same protocol was applied, but the solution was contained in a HPLC-MS vial, which was then inserted in the injection system. The detector was set to measure Total Ionic Current, and the signal was filtered to show only the m/z of interest. The chromatograms were analyzed with the instrument software. The determination of compound stability during repeated photoisomerization, was obtained with cycles of 3 min of 380-nm illumination, 3 min of 430 nm illumination, and 3 min of 500 nm illumination, interspersed with absorption measurement. For the qualitative determination of the thermal relaxation of the *cis* isomer, UV-Vis absorption spectra were recorded during 3 h, with analyzing pulses of 1 s every 5 min at 340 nm.

UV-VIS spectra. Measurements of UV-VIS spectra were recorded using a UV−1800 UV-vis spectrophotometer (Shimadzu, Kyoto, Japan). Fits of UV-Vis spectroscopy data were generated using GraphPad Prism 8 software. Samples were 50 micromolar in aqueous solution, with 0.5% DMSO.

Two-photon isomerization. To achieve photoconversion, 200 μL of a 50 μM solution of **CPZ−2** were transferred in the well of a Petri dish, fitted with wet paper strips in the walls, in order to limit evaporation. The closed chamber was mounted in the stage of a LSM 880 Confocal Microscope (Carl Zeiss). The solution was then irradiated using a pulsed Ti:Sapphire Laser emitting at 760 nm and set to a medium output of 1 mW. The stage was programmed to perform a fast raster scanning in the whole field of view of the microscope in the X,Y coordinates, centered at the center of the well. The Z coordinate was set to be half the height of the liquid in the well. Every 30 min 3 μL of the solution were taken and diluted in 27 μL of solution, yielding a 5 μM solution which was then analyzed with HPLC-MS, using SIR mode, measuring currents at m/z 429 ± 0.2.

7.3. Synthetic protocols and analytical data

7.3.1. Methyl 4-nitrobenzoate (2 h)

2 g (10.80 mmol) of the commercially available 2-fluoro−4-nitrobenzoic acid **1h** was dissolved in 10 ml of methanol; to the solution were added 5.8 ml (10.80 mmol) of sulfuric acid. The resulting mixture was stirred on gentle reflux (80 °C) overnight. The resulting mixture was then cooled, and the excess methanol was evaporated under reduced pressure. The residue was diluted with ethyl acetate and washed three times with saturated sodium bicarbonate solution. The ethyl acetate solution was then dried over anhydrous sodium sulphate and evaporated under reduced pressure, to give 2.15 g (10.80 mmol) of **2h**. White solid, quantitative yield. m.p.: 94–95 °C. R_f: 0.83 (1:1 cyclohexane/ethyl acetate). ^{1}H NMR: (300 MHz, cdcl$_3$) δ 8.29 (d, *J* = 9.0 Hz, 2 H), 8.20 (d, *J* = 9.0 Hz, 2 H), 3.97 (s, 3 H). ^{13}C NMR: (75 MHz, cdcl$_3$) δ 165.1 (s), 150.5 (s), 135.5(s), 130.6(s), 123.4, 52.7 (s).

7.3.2. Methyl 2-fluoro−4-nitrobenzoate (2f)

2 g (10.80 mmol) of the commercially available 2-fluoro−4-nitrobenzoic acid **1f** was dissolved in 10 ml of methanol; to the solution were

added 5.8 ml (10.80 mmol) of sulfuric acid. The resulting mixture was stirred on gentle reflux conditions, at 80 °C, overnight. The mixture was then cooled, and the excess methanol was evaporated under reduced pressure. The residue was diluted with ethyl acetate and washed three times with saturated sodium bicarbonate solution. The ethyl acetate solution was then dried over anhydrous sodium sulphate and evaporated under reduced pressure, to give 2.15 g (10.80 mmol) of **2f**. White solid, quantitative yield. m.p.: 75.5 °C. R_f: 0.83 (1:1 cyclohexane/ethyl acetate). ^{1}H NMR: (300 MHz, cdcl$_3$) δ 8.19–8.08 (m, 2 H), 7.93–7.82 (m, 1 H), 4.35 (s, 2 H). ^{13}C NMR: (75 MHz, cdcl$_3$) δ 163.90 (s), 160.27 (s), 151.93 (s), 133.89 (s), 124.95 (s), 119.87 (s), 113.73 (d, J = 30.1 Hz), 53.91 (s).

7.3.3. 4-Nitrobenzohydrazide (3h)

2.19 g (11 mmol) of **2h** were dissolved in a minimal amount of methanol, and the solution was cooled to 0 °C in an ice bath. To the cooled mixture were added 2.4 ml (2.47 g, 48.39 mmol) of 98% hydrazine hydrate, and the resulting solution was stirred at 0 °C for 30 min, and then heated to 60 °C, and kept at that temperature and stirred for 4 h. The flask was then cooled and kept at −17 °C overnight to allow precipitation of the product, which was filtered and washed with cold ethanol, to obtain 1.41 g (7.07 mmol) of **3h**. Yellow solid, yield: 64%. m.p.: 218 °C (decomposition). R_f: 0.44 (98:2 dichloromethane/methanol). ^{1}H NMR: (300 MHz, cdcl$_3$) δ 8.32 (d, J = 8.0 Hz, 2 H), 7.93 (d, J = 8.1 Hz, 2 H), 7.48 (s, 1 H),4.35 (s, 2 H). ^{13}C NMR: (75 MHz, cdcl$_3$) δ 163 (s), 148.9 (s), 139.0 (s), 128.4 (s), 123.4 (s).

7.3.4. 2-Fluoro−4-nitrobenzohydrazide (3f)

2.19 g (11 mmol) of **2f** were dissolved in a minimal amount of methanol, and the obtained solution was cooled to 0 °C in an ice bath. To the cooled mixture were added 2.4 ml (2.47 g, 48.39 mmol) of 98% hydrazine hydrate, and the resulting solution was stirred at 0 °C for 30 min, and then heated to 60 °C, and kept at that temperature under stirring for 4 h. The flask was then cooled and kept at −17 °C overnight to allow precipitation of the product, which was filtered and washed several times with cold ethanol, to obtain 1.41 g (7,07 mmol) of **3f**. Yellow solid, yield: 64%. m.p.: 203°C (decomposition). R_f: 0.44 (98:2 DCM/MeOH). ^{1}H NMR: (300 MHz, cd$_3$od) δ 8.19–8.08 (m, 2 H), 7.93–7.82 (m, 1 H). ^{13}C NMR: (75 MHz, cdcl$_3$) δ 162.37 (d, J = 4.0 Hz), 159.72 (d, J = 252.3 Hz),150.38 (d, J=9.8 Hz), 133.27 (d, J = 3.0 Hz), 124.95 (d, J = 13.6 Hz), 119.78 (d, J = 3.5 Hz), 112.21 (d, J = 30.1 Hz).

7.3.5. 5-(4-Nitrophenyl)−1,3,4-oxadiazole−2-thiol (4 h)

1.41 g (7.07 mmol) of **3h** were dissolved in ethanol. To the solution were added 934 μl of CS_2 (1.18 g, 15.54 mmol) and 1.08 ml of triethylamine (786 mg, 7.77 mmol). Upon addition the solution turned red. The reaction was stirred under reflux conditions (around 90 °C) overnight. The solution was then cooled overnight at −17 °C, allowing for the precipitation of an orange solid, which was filtered and washed with cold ethanol. The filtrate was dissolved with ethyl acetate and washed two times with hydrochloric acid 0.1 M. The organic phase was then washed with brine, dried over anhydrous sodium sulphate, and the solvent was evaporated under reduced pressure, to obtain **4h** as a yellow solid. Yellow solid, yield: 73%. m.p.: 202 °C. R_f: 0.3 (7:3 cyclohexane/ethyl acetate, 1% Acetic acid). ^{1}H NMR: (300 MHz, cdcl$_3$) δ 8.40 (d, J = 8.5 Hz, 2 H), 8.17 (d, J = 8.3 Hz, 2 H). ^{13}C NMR: (75 MHz, DMSOd$_6$) δ 124.6 (s), 127.4 (s), 128.0 (s), 149.1 (s), 158.9 (s), 77.8 (s).

7.3.6. 5-(2-Fluoro−4-nitrophenyl)−1,3,4-oxadiazole−2-thiol (4 f)

1.41 g (7.07 mmol) of **3f** were dissolved in ethanol. To the solution were added 934 μl of CS_2 (1.18 g, 15.54 mmol) and 1.08 ml of triethylamine (786 mg, 7.77 mmol). Upon addition the solution turned red. The reaction was stirred under reflux conditions, at 90 °C, overnight. The solution was then cooled overnight at −17 °C, allowing for the precipitation of an orange solid, which was filtered and washed with cold ethanol. The filtrate was dissolved with ethyl acetate and washed two times with hydrochloric acid 0.1 M. The organic phase was then washed with brine, dried over anhydrous sodium sulphate, and the solvent was evaporated under reduced pressure, to afford **4f** as a yellow solid. Yellow solid, yield: 57%. m.p.: 193 °C. R_f: 0.3 (7:3 cyclohexane/ethyl acetate, 1% acetic acid). ^{1}H NMR: (300 MHz, cdcl$_3$) δ 11.50 (s, 1 H), 8.25–8.10 (m, 3 H). ^{13}C NMR: (75 MHz, cdcl$_3$) δ 177.50 (s), 159.60 (d, J = 265.9 Hz), 155.99 (d, J = 6.5 Hz), 150.54 (d, J = 8.2 Hz), 129.89 (s), 119.88 (d, J = 4.2 Hz), 116.49 (d, J = 11.4 Hz), 113.17 (d, J = 25.5 Hz).

7.3.7. 2-(Benzylthio)−5-(4-nitrophenyl)−1,3,4-oxadiazole (5 h)

973 mg (3.88 mmol) of **4h** were dissolved in 3 ml of DMF, to give a red solution. To the resulting solution were added 3.88 ml of 1 M NaOH (3.88 mmol) and 702 μl (5.90 mmol) of benzyl bromide. Upon addition a yellow precipitate formed. The resulting suspension was stirred for 2 h at room temperature. The suspension was diluted with water, causing more precipitation of the product, which was filtered. The filtrate was dissolved with ethyl acetate and evaporated under reduced pressure. The resulting solid was washed with cold ethanol to obtain 1.11 g (3.35 mmol) of pure **5h**. White solid, yield 86%. m.p.: 201 °C. R_f: 0.55 (6:4 cyclohexane/ethyl acetate). ^{1}H NMR: (300 MHz, cdcl$_3$) δ 8.36 (d, J = 8.5 Hz, 2 H), 8.18 (d, J = 9.0 Hz, 2 H), 7.47 (d, J = 6.9 Hz, 2 H), 7.42 – 7.28 (m, 3 H), 4.56 (s, 2 H). ^{13}C NMR: (75 MHz, cdcl$_3$) δ 165.77 (s), 164.19 (s), 149.60 (s), 135.38 (s), 129.31 (s), 129.02 (s), 128.42 (s), 127.66 (s), 124.54 (s), 37.02 (s).

7.3.8. 2-(Benzylthio)−5-(2-fluoro−4-nitrophenyl)−1,3,4-oxadiazole (5 f)

973 mg (3.88 mmol) of **4f** were dissolved in 3 ml of DMF, to the resulting solution were added 3.88 ml of 1 M NaOH (3.88 mmol) and 702 μl (5.90 mmol) of benzyl bromide. Upon addition a yellow precipitate formed. The resulting suspension was stirred for 2 h at room temperature. The suspension was diluted with water, causing the precipitation of the product, which was filtered. The filtrate was diluted with ethyl acetate and evaporated under reduced pressure. The resulting solid was washed with cold ethanol to obtain 1.11 g (3.35 mmol) of pure **5f**. White solid, yield: 83%. m.p.: 194 °C. R_f: 0.55 (6:4 cyclohexane/ethyl acetate). ^{1}H NMR: (300 MHz, cdcl$_3$) δ 8.25–8.10 (m, 3 H), 7.50–7.21 (m, 5 H), 4.78 (s, 2 H). ^{13}C NMR: (75 MHz, cdcl$_3$) δ 166.20 (s), 161.01 (d, J = 5.4 Hz), 157.55 (s), 150.25 (d, J = 8.3 Hz), 135.33 (s), 130.38 (d, J = 1.7 Hz), 129.30 (s), 128.99 (s), 128.39 (s), 119.83 (d, J = 4.1 Hz), 118.01 (d, J = 12.1 Hz), 113.35 (s), 113.00 (s), 36.95 (s).

7.3.9. 2-(Benzylsulfonyl)−5-(4-nitrophenyl)−1,3,4-oxadiazole (6 h)

1.11 g (3.35 mmol) of **5h** were dissolved in the minimal amount of glacial acetic acid. The solution was then cooled to 10 °C, and to the cooled solution were added, dropwise and with strong stirring, 14.07 ml of 5% aqueous solution on $KMnO_4$ (703.53 mg, 4.45 mmol). Upon addition, after an initial discoloration, the mixture becomes thicker and thicker due to the precipitation of MnO_2. The slurry was allowed to react for 20 min. If necessary, more $KMnO_4$ was added up until the total consumption of the reactant, and at that point the reaction was quenched with saturated sodium metabisulphite solution (around 15 ml). Upon quenching the black precipitate dissolves, and a white precipitate forms. This was filtered and washed with cold water several times, yielding 572 mg (1.66 mmol) of **6h**. Off-white solid, yield 47%. m.p.: 233 °C (decomposition). R_f: 0.53 (6:4 Cyclohexane Ethyl acetate). ^{1}H NMR: (300 MHz, cdcl$_3$) δ 8.39 (d, J = 8.8 Hz, 2 H), 8.21 (d, J = 8.7 Hz, 2 H), 7.38 (s, 4 H), 4.84 (s, 2 H). ^{13}C NMR: (75 MHz, cdcl$_3$) δ 164.87 (s), 162.33 (s), 150.59 (s), 131.43 (s), 130.10 (s), 129.99 (s),129.42 (s), 128.87 (s), 127.51 (s), 124.70 (s), 62.33 (s).

7.3.10. 2-(Benzylsulfonyl)−5-(2-fluoro−4-nitrophenyl)−1,3,4-oxadiazole (6 f)

1.11 g (3.35 mmol) of **5f** were dissolved in the minimal amount of glacial acetic acid. The solution was then cooled to 10 °C, and to the cooled solution were added, dropwise and with strong stirring, 14.07 ml

of 5% aqueous solution on $KMnO_4$ (703.53 mg, 4.45 mmol). Upon addition, after an initial discoloration, the mixture becomes thicker and thicker due to the precipitation of MnO_2. The slurry was allowed to react for 20 min. If necessary, more $KMnO_4$ was added up until the total consumption of the reactant, and at that point the reaction was quenched with saturated sodium bisulfite solution (about 15 ml). Upon quenching the black precipitate dissolves, and a white precipitate forms. This was filtered and washed with cold water several times, yielding 572 mg of **6f**. Off-white solid, yield: 47%. m.p.: 210 °C (decomposition). R_f: 0.53 (6:4 cyclohexane/ethyl acetate). ^{1}H NMR: (300 MHz, cdcl$_3$) δ 8.23–8.10 (m, 3 H), 7.54–7.22 (m, 5 H), 4.85 (s, 2 H). ^{13}C NMR: (75 MHz, cdcl$_3$) δ 131.42 (s), 130.13 (s), 129.44 (s), 120.01 (d, J = 4.3 Hz), 113.59 (s), 113.25 (s), 77.58 (s), 62.32 (s).

7.3.11. N-(3-Morpholinopropyl)−5-(4-nitrophenyl)−1,3,4-oxadiazol−2-amine (7 h)

572 mg (1.57 mmol) of **6h** were dissolved in around 9 ml of 1,4-dioxane. To the stirred solution at room temperature were added dropwise 575 μl (3.94 mmol) of *N*-(3-aminopropyl)morpholine. Upon addition the solution turned orange. The reaction was monitored with TLC (1:1 cyclohexane/ethyl acetate to monitor the reactant consumption, 9:1 dichloromethane/methanol to monitor product formation). Upon completion, the solution was diluted with ethyl acetate and extracted twice with water. The organic phase was then dried over anhydrous sodium sulphate and evaporated completely, giving a yellow solid. This was washed a few times with cold cyclohexane, to yield 500 mg (1.42 mmol) of **7h**. Yellow solid, yield: 91%. m.p.: 60 °C. R_f: 0.5 (9:1 DCM/MeOH). ^{1}H NMR: (300 MHz, cdcl$_3$) δ 8.31 (d, J = 9.0 Hz, 2 H), 8.06 (d, J = 8.9 Hz, 2 H), 7.18 (t, J = 4.7 Hz, 1 H), 3.85 – 3.75 (m, 4 H), 3.66 – 3.55 (m, 2 H), 2.70 – 2.62 (m, 2 H), 2.58 (s, 4 H), 1.98 – 1.85 (m, 2 H). ^{13}C NMR: (75 MHz, cdcl$_3$) δ 164.17 (s), 157.26 (s), 148.68 (s), 130.22 (s), 126.40 (s), 124.41 (s), 67.11 (s), 58.13 (s), 53.79 (s), 44.14 (s), 24.24 (s).

7.3.12. 5-(2-Fluoro−4-nitrophenyl)-N-(3-morpholinopropyl)−1,3,4-oxadiazol−2-amine (7 f)

572 mg (1.57 mmol) of **6f** were dissolved in around 9 ml of 1,4-dioxane. To the stirred solution at room temperature were added dropwise 575 μl (3.94 mmol) of *N*-(3-aminopropyl)morpholine. Upon addition the solution turned orange. The reaction was monitored with TLC (1:1 cyclohexane/ethyl acetate to monitor the reactant consumption, 9:1 dichloromethane/methanol to monitor product formation). Upon completion the solution was diluted with ethyl acetate and washed twice with water. The organic phase was then dried over anhydrous sodium sulphate and evaporated completely, giving a yellow solid. This was washed five times with cold cyclohexane, to yield 500 mg (1.42 mmol) of **7f**. Yellow solid, yield 91%. m.p.: 55 °C. R_f: 0.5 (9:1 DCM/MeOH). ^{1}H NMR: (300 MHz, cdcl$_3$) δ 8.28 – 7.97 (m, 3 H), 7.36 (s, 1 H), 3.75 (t, J = 4.6 Hz, 4 H), 3.58 (t, J = 5.8 Hz, 2 H), 2.59 (t, J = 6.0 Hz, 2 H), 2.52 (s, 4 H), 1.86 (d, J = 6.0 Hz,2 H). ^{13}C NMR: (75 MHz, cdcl$_3$) δ 129.41 (d, J = 2.4 Hz), 119.76 (d, J = 4.0 Hz), 113.22 (s),112.87 (s), 77.58 (s), 77.16 (s), 76.74 (s), 67.19 (s), 58.33 (s), 53.84 (s), 44.38(s), 24.18 (s).

7.3.13. 5-(4-Aminophenyl)-N-(3-morpholinopropyl)−1,3,4-oxadiazol−2-amine (8 h)

250 mg (749.97 μmol) of **7 h** were dissolved in the minimal amount of ethanol. 25 mg of Pd/C 10% (10% mass ratio with respect to the reagent) was wetted with fresh ethanol in a round bottom flask. To the slurry was added the solution of **7 h**. The resulting solution, with suspended Pd/C, was stirred under an H_2 atmosphere overnight, affording a colorless solution. The obtained product was highly air-sensitive; therefore, the remainder of the procedure was carried out under an inert atmosphere. After filtering off the Pd/C, the clear solution was evaporated under reduced pressure, yielding a white residue. The crude product was directly used in the subsequent step without further purification. White solid, yield unknown. Routine analyses were not performed since the compound was too unstable.

7.3.14. 5-(4-Amino−2-fluorophenyl)-N-(3-morpholinopropyl)−1,3,4-oxadiazol−2-amine (8 f)

500 mg (1,72 mmol) of **7 f** were dissolved in the minimal amount of ethanol. 50 mg of Pd/C 10% (10% mass ratio with respect to the reagent) was wetted with fresh ethanol in a round bottom flask. To the slurry was added the solution of **7 f**. The resulting solution, containing suspended Pd/C, was stirred under an H_2 atmosphere overnight to afford a colorless solution. The product proved extremely air-sensitive; therefore, the remainder of the procedure was carried out under an inert atmosphere. The Pd/C was filtered off, and the clear solution was evaporated under reduced pressure, yielding a white powder. The obtained powder was used in the next step without further purification. White solid, yield unknown. Routine analyses were not performed since the compound was too unstable.

7.3.15. 2-Fluoronitrosobenzene (10 h)

434 μl (4.5 mmol) of 2-fluoroaniline **9 h** was dissolved in 10 ml of dichloromethane. 5.53 g (9 mmol) of Oxone® were dissolved in 40 ml of water. The two solutions were combined in a round bottom flask, and the biphasic system was vigorously stirred under inert atmosphere and with protection from light for 24 h, resulting in a deep green organic layer and a bright red aqueous layer. The two were separated in a separating funnel, and the aqueous layer was extracted twice with 10 ml of dichloromethane. The two portions were reunited with the dichloromethane solution obtained from the reaction and altogether were washed with 15 ml of HCl 0.1 M and then washed extensively with saturated sodium bicarbonate solution. The dichloromethane was then removed under reduced pressure, and the resulting brown solid was passed through a silica gel plug (9:1 DCM/MeOH). The solution was then distilled under reduced pressure to yield a yellow solid. The dichloromethane solutions obtained by distillation were evaporated at room temperature and pressure, to yield a white solid. The two products combined were used in the next step. Yellow solid, yield: 40%. m.p.: 68–70 °C. R_f: 0.3 (9:1 cyclohexane/ethyl acetate). ^{1}H NMR: (300 MHz, CD_3Cl) δ 6.49 (ddd, J_1=10.5 Hz, J_2=8.5 Hz, J_3=1.8 Hz, 1 H), 7.14 (t, J=7.0 Hz,1 H), 7.51 (ddd, J_1=8.0 Hz, J_2=7.0 Hz, J_3=1.1 Hz,1 H), 7.76–7.68 (m, 1 H).

7.3.16. 1,3-Difluoro−2-nitrosobenzene (10 f)

500 μl (4.65 mmol) of 2,6-difluoroaniline **9 f** was dissolved in 10 ml of dichloromethane. 5.71 g (9.29 mmol) of Oxone® were dissolved in 40 ml of water. The two solutions were combined in a round bottom flask, and the biphasic system was vigorously stirred under inert atmosphere and with protection from light for 24 h, resulting in a deep green organic layer and a bright red aqueous layer. The two were separated in a separating funnel, and the aqueous layer was extracted twice with 10 ml of dichloromethane. The two portions were reunited with the dichloromethane solution obtained from the reaction and altogether were washed with 15 ml of HCl 0.1 M and then washed extensively with saturated sodium bicarbonate solution. The organic layer was then dried over sodium sulphate and concentrated under reduced pressure to yield 500 mg of **10 f** as a brown solid. Brown solid, yield: 90%. m.p.: 199 °C. R_f: 0.55 (1:1 cyclohexane/ethyl acetate). ^{1}H NMR: (300 MHz, $(CD_3)_2CO$) δ 7.92 (m, 1 H), 7.37 (t, J = 8.9 Hz, 2 H). ^{13}C NMR: (75 MHz, $(CD_3)_2CO$) δ 154.2 (d, J = 267 Hz), 139.6 (t, J = 11.4 Hz), 114.1 (d, J = 23.8 Hz).

7.3.17. 2-(3-Fluoro−4-(5-((3-morpholinopropyl)amino)−1,3,4-oxadiazol−2-yl)phenyl)−1-(2-fluorophenyl)diazene 1-oxide (undesired azoxybenzene derivative of CPZ−1)

In an inert atmosphere a theoretical 273 mg of **8 f** (899 μmol) were dissolved in the minimal amount of 6:6:1 trifluoroacetic acid/acetic acid/toluene, yielding a colorless solution. 113 mg of **10 h** (899 μmol)

were dissolved in the minimal amount of the same solvent, yielding a green solution. The two solutions were combined dropwise under inert atmosphere and stirred overnight. During the first hour it was observed a darkening of the solution, up to becoming black. After 15 h of stirring the solution was placed in an ice bath and neutralized with a saturated sodium carbonate solution. The aqueous solution was then extracted 5 times with DCM, and the organic layers were combined and evaporated under reduced pressure. The resulting orange solid was purified through column chromatography (9:1 DCM/MeOH), to yield 50 mg (122 μmol) of the undesired azoxybenzene as a bright yellow solid. Yellow solid, yield: 14%. m.p.: 137 °C. R_f: 0.83 (8:2 DCM/MeOH). ^{1}H NMR: (300 MHz, $(CD_3)_2CO$)) δ 8.41 – 8.28 (m, 2 H), 8.28 – 8.16 (m, 2 H), 7.60–7.48 (m, 1 H), 7.46 – 7.32 (m, 2 H), 7.29 (s, 1 H), 3.65 (t, J = 4.6 Hz, 4 H), 3.53 dd, J = 12.3, 6.5 Hz, 2 H), 2.52 (t, J = 6.6 Hz, 2 H), 2.46 (s, 4 H), 1.91 (p, J = 6.6 Hz, 2 H). ^{13}C NMR: (101 MHz, cdcl$_3$) δ 164.11 (s), 160.00 (s), 158.26 (s), 154.46 (d, J = 5.6 Hz), 149.68 (s), 132.14 (d, J = 8.6 Hz), 131.05 (d, J = 8.5 Hz), 128.91 (s), 124.20 (s), 124.09 (d, J = 3.8 Hz), 118.66 (d, J = 3.7 Hz), 116.89 – 116.08 (m), 112.02 (s), 111.75 (s),77.27 (d, J = 11.7 Hz), 76.70 (s), 67.01 (s), 58.04 (s), 53.70 (s), 44.05 (s), 24.23 (s).

7.3.18. 5-(4-((2,6-Difluorophenyl)diazenyl)phenyl)-N-(3-morpholinopropyl)−1,3,4-oxadiazol−2-amine (CPZ−2)

In an inert atmosphere a theoretical amount of 227.51 mg of **8 h** (749.95 μmol) were dissolved in the minimal amount of 6:6:1 trifluoroacetic acid/acetic acid/toluene mixture, yielding a colorless solution. 107 mg of **10 f** (749.95 μmol) were dissolved in the minimal amount of the same solvent, yielding a brown solution. The two solutions were combined dropwise under inert atmosphere and stirred overnight. During the first hour it was observed a darkening of the solution, up to becoming black. After 15 h of stirring the solution was placed in an ice bath and the pH was raised to 10 with a saturated sodium carbonate solution. The solution was then extracted 5 times with equal volume of DCM, which was dried and evaporated under reduced pressure. The resulting brown solid was purified through column chromatography (9:1 DCM/MeOH), to yield 30 mg of **CPZ−2** as a deep red solid. Red solid, yield: 9%. m.p.: 157 °C. R_f: 0.83 (8:2 DCM/MeOH). ^{1}H NMR: (300 MHz, $CDCl_3$) δ 8.09 – 7.95 (m, 3 H, *trans isomer*), 7.83 – 7.79 (m, *cis isomer*), 7.40 – 7.28 (m, 1 H), 7.05 (t, J = 8.7 Hz, 2 H, *trans isomer*), 6.95 (br s, 1 H), 6.82 – 6.76 (m, *cis isomer*), 3.83 – 3.73 (m, 4 H), 3.58 (s, 2 H), 2.63 (t, J = 6.1 Hz, 2 H), 2.57 (s, 4 H), 1.90 (dt, J = 12.3, 6.1 Hz, 2 H). ^{13}C NMR: (101 MHz, cdcl$_3$) δ 163.87 (s), 158.45 (s), 156.45 (dd, J = 260.2, 4.1 Hz), 154.02 (s), 131.00 (t, J = 10.3 Hz), 127.37 (s), 126.62 (s), 126.31 (s), 123.66 (s), 119.48 (s), 112.74 (d, J = 24.1 Hz), 66.62 (s), 57.58 (s), 53.60 (s), 43.37 (s), 24.23 (s).

7.3.19. 1-(2,6-Difluorophenyl)−2-(3-fluoro−4-(5-((3-morpholinopropyl)amino)−1,3,4-oxadiazol−2-yl)phenyl)diazene 1-oxide (undesired azoxybenzene derivative of CPZ−3)

In an inert atmosphere a theoretical amount of 227.51 mg of **8 f** (749.95 μmol) were dissolved in the minimal amount of 6:6:1 trifluoroacetic acid/acetic acid/toluene mixture, yielding a colorless solution. 107 mg of **10 f** (749.95 μmol) were dissolved in the minimal amount of the same solvent, yielding a brown solution. The two solutions were combined dropwise under inert atmosphere and stirred overnight. During the first hour it was observed a darkening of the solution, up to becoming black. After 15 h of stirring the solution was placed in an ice bath and the pH was raised to 10 with a saturated sodium carbonate solution. The solution was then extracted 5 times with equal volume of DCM, which was dried and evaporated under reduced pressure. The resulting black solid was purified through column chromatography (9:1 DCM/MeOH), and the impure fraction was analyzed with HPLC-MS. Since the product was not the one expected, it was decided to not proceed further with the characterization. LCMS analysis: ESI m/z $[M + H]^+$ calculated 447.43, found 463.43 (azoxybenzene derivative); retention time: 97.2 s.

7.4. Radioligand binding assays

The binding affinity of **CPZ−2** at nicotinic acetylcholine receptors was assessed using radioligand binding assays performed by Eurofins Panlabs Discovery Services.

Chemicals and Reagents. Radioligands specific for each nicotinic acetylcholine receptor (nAChR) subtype were obtained and utilized as follows: [^{125}I] α-Bungarotoxin for α1-containing nAChR; [^{125}I] Epibatidine for α3β4 nAChR; [^{3}H] Cytisine for α4β2 nAChR; [^{3}H] Methyllycaconitine for α7 nAChR. The vehicle for all experiments was 1.0% dimethyl sulfoxide (DMSO). All reagents were of analytical grade.

Cell Lines and Membranes. Human recombinant cell lines were used as the source of specific nAChRs: α1-containing nAChRs were expressed in human RD cells; α3β4 nAChRs were expressed in CHO-K1 cells; α4β2 and α7 nAChRs were expressed in SH-SY5Y cells. Membranes were prepared from these cell lines according to standard protocols to ensure receptor integrity.

Binding Assays. Binding assays were performed under the following conditions. α1-containing nAChRs: Assays were conducted with 0.6 nM [^{125}I] α-Bungarotoxin in an incubation buffer containing 147 mM NaCl, 4 mM KCl, and 2.2 mM $CaCl_2$. Incubation was performed at 25 °C for 2 h. α3β4 nAChRs: Assays used 0.05 nM [^{125}I] Epibatidine in a Tris-HCl buffer (50 mM, pH 7.4). Incubation was carried out at 25 °C for 1 h. α4β2 nAChRs: 0.6 nM [^{3}H] Cytisine was used in a Tris-HCl buffer supplemented with NaCl, KCl, MgCl2, and $CaCl_2$. Incubation was at 4 °C for 2 h. α7 nAChRs: Assays used 2.0 nM [^{3}H] Methyllycaconitine in a phosphate buffer (pH 7.4) containing 0.1% bovine serum albumin (BSA). Incubation was performed at 25 °C for 2 h. Non-specific binding was determined using the respective non-radioactive ligands at high concentrations (1.0 μM for α1-containing nAChRs, 10.0 μM for α3β4, α4β2, and α7 nAChRs).

Data Analysis. IC_{50} values were determined via non-linear least squares regression analysis using MathIQ™ software. Inhibition constants (K_i) were calculated using the Cheng-Prusoff equation, incorporating the observed IC_{50} values, radioligand concentrations, and historical K_D values. Hill coefficients (nH) were also calculated to assess the binding curve's slope. Experiments were performed in duplicate, and results were averaged for analysis.

Statistical Analysis. Binding data were considered significant if inhibition or stimulation reached ≥ 50% of maximum binding. Experimental replicates were evaluated to ensure consistency and reproducibility.

7.5. Behavioral experiments in zebrafish larvae

Wild type zebrafish embryos (Tüpfel long-fin strain) were purchased from the animal facility of the Barcelona Biomedical Research Park (PRBB) and raised in darkness at 28.5 °C in UV filtered tap water in Petri dishes (daily cleaned and refilled). Animal development was checked every 24 h. Behavioral studies were conducted 2 days post fertilization (hpf) in darkness. Vehicle and compounds were added with a multichannel pipette. Movements were recorded and analyzed using the Zebrabox (ViewPoint Life Science, Lyon, FR).

The embryos were manually dechorionated, transferred to fresh water, and randomly divided into 3 groups (10 per group). Individual embryos were placed in separate wells of a 96-well plate, each containing 50 μl of fresh sterilized water and 50 μl *trans*-CPZ (pre-illuminated for 5 min with blue light at 455 nm) or *cis*-CPZ (pre-illuminated for 5 min with UV light at 365 nm) dissolved in water with 0.5% DMSO in two different concentrations (5 μM and 10 μM). To measure the distance moved, the plate was inserted into the Zebrabox (ViewPoint Life Sciences, Lyon, France), and the first period of recording was made. Afterward, 50 μL of nicotine stock solution was added to reach final nicotine concentrations of 60 μM or 120 μM, and a second recording period was started. Statistical analyses were performed in GraphPad Prism 9 using ordinary two-way ANOVA followed by Tukey's multiple

comparisons test.

7.6. Computational studies

Ligands were designed using Chem3D and subjected to geometrical optimization and vibrational frequencies calculations in Gaussian 16 using DFT with B3LYP functional and 6–31 + g (d,p) basis set [49]. Solvation energy was accounted for using the CPCM model, using water as an implicit solvent. All docking simulations were performed using the optimized ligands and the cryo-EM structure of the α7 nAChR bound to alpha-bungarotoxin in the resting state (PDB ID: 7KOO) [45]. The downloaded structures were refined by reconstructing the disulfide bond between Cysteines 189 and 190 and adding missing hydrogen atoms using H + + [50]. To ensure compatibility with physiological pH, Asp, Glu, Lys, and Arg residues were treated as ionized, while Cys and His were considered neutral by default. The finalized protein structures underwent minimization with the backbone atoms constrained to retain the experimental folding. Docking simulations were carried out using PLANTS algorithm in the VegaZZ suite of programs, restricting the search space to residues contained in a 5 Å radius, centered on Arg 36 of the bound (and deleted) alpha bungarotoxin. For each ligand, 10 docking poses were generated and ranked with the ChemPLP scoring function, using a speed setting of 1. The poses showing the best binding score for each ligand were selected for further investigations, excluding results which resulted in unfavorable bumps between the ligand and the receptor [51]. Docking simulation images were prepared using Biovia Discovery Studio 2020.

CRediT authorship contribution statement

Nayeli Fernanda Pérez-Pérez: Writing – review & editing, Methodology, Investigation, Formal analysis. **Claudio Papotto:** Writing – review & editing, Methodology, Investigation, Formal analysis, Data curation. **Carlo Matera:** Writing – review & editing, Writing – original draft, Supervision, Methodology, Investigation, Formal analysis, Data curation, Conceptualization. **Pau Gorostiza:** Writing – review & editing, Writing – original draft, Supervision, Funding acquisition, Formal analysis, Data curation, Conceptualization. **Alexandre M.J. Gomila:** Writing – review & editing, Methodology, Investigation, Formal analysis. **Mercè Cases:** Writing – review & editing, Methodology, Investigation, Formal analysis. **Rosalba Sortino:** Writing – review & editing, Methodology, Investigation, Formal analysis, Data curation. **Clelia Dallanoce:** Writing – review & editing, Supervision, Conceptualization. **Marco De Amici:** Writing – review & editing, Supervision, Conceptualization. **Francesco Calzaferri:** Writing – review & editing, Methodology, Investigation. **Hyojung Lee:** Methodology, Investigation.

Declaration of Generative AI and AI-assisted technologies in the writing process

During the preparation of this work the authors used ChatGPT (OpenAI) in order to improve the language, readability, and overall wording of the manuscript. After using this tool, the authors reviewed and edited the content as needed and take full responsibility for the content of the published article.

Funding declaration

This research received funding from the European Union Research and Innovation Programme Horizon 2020 – Human Brain Project SG3 (945539), DEEPER (ICT-36-2020-101016787), European Innovation Council Pathfinder Open (PHOTOTHERAPORT, 101130883), Agency for Management of University and Research Grants/Generalitat de Catalunya (CERCA Programme; 2021-SGR-01410), Ministry of Science and Innovation grants PID2019–111493RB-I00 (DEEP RED) and PID2022–142609OB-I00 (EPILLUM).

Declaration of Competing Interest

The authors declare that they have no known competing financial interests or personal relationships that could have appeared to influence the work reported in this paper.

Appendix A. Supporting information

Supplementary data associated with this article can be found in the online version at doi:10.1016/j.biopha.2026.119727.

Data availability

Data will be made available on request.

References

[1] A. Chatzidaki, N.S. Millar, Allosteric modulation of nicotinic acetylcholine receptors, Biochem. Pharmacol. 97 (2015) 408–417, https://doi.org/10.1016/j.bcp.2015.07.028.
[2] K.T. Dineley, A.A. Pandya, J.L. Yakel, Nicotinic ACh receptors as therapeutic targets in CNS disorders, Trends Pharmacol. Sci. 36 (2015) 96–108, https://doi.org/10.1016/j.tips.2014.12.002.
[3] D. Paterson, A. Nordberg, Neuronal nicotinic receptors in the human brain, Prog. Neurobiol. 61 (2000) 75–111.
[4] S. Wonnacott, S. Wonnacott, Presynaptic nicotinic ACh receptors, Trends Neurosci. 20 (1997) 92–98.
[5] R. Faghih, M. Gopalakrishnan, C.A. Briggs, Allosteric Modulators of the alpha7 Nicotinic Acetylcholine Receptor, J. Med. Chem. 51 (2008) 701–712.
[6] A. De Jaco, L. Bernardini, J. Rosati, A.M. Tata, Alpha-7 nicotinic receptors in nervous system disorders: from function to therapeutic perspectives, Cent. Nerv. Syst. Agents Med. Chem. 17 (2016), https://doi.org/10.2174/1871524916666160729111446.
[7] G. Winterer, J. Gallinat, J. Brinkmeyer, F. Musso, J. Kornhuber, N. Thuerauf, D. Rujescu, R. Favis, Y. Sun, M.A. Franc, S. Ouwerkerk-Mahadevan, L. Janssens, M. Timmers, J.R. Streffer, Allosteric alpha-7 nicotinic receptor modulation and P50 sensory gating in schizophrenia: a proof-of-mechanism study, Neuropharmacology 64 (2013), https://doi.org/10.1016/j.neuropharm.2012.06.040.
[8] J.A. Micoulaud-Franchi, F. Vaillant, R. Lopez, P. Peri, A. Baillif, L. Brandejsky, M. L. Steffen, L. Boyer, R. Richieri, M. Cermolacce, S. Bioulac, M. Aramaki, P. Philip, C. Lancon, J. Vion-Dury, Sensory gating in adult with attention-deficit/hyperactivity disorder: event-evoked potential and perceptual experience reports comparisons with schizophrenia, Biol. Psychol. 107 (2015), https://doi.org/10.1016/j.biopsycho.2015.03.002.
[9] E.V. Orekhova, T.A. Stroganova, A.O. Prokofyev, G. Nygren, C. Gillberg, M. Elam, Sensory gating in young children with autism: relation to age, IQ, and EEG gamma oscillations, Neurosci. Lett. 434 (2008), https://doi.org/10.1016/j.neulet.2008.01.066.
[10] H.O. Kalkman, D. Feuerbach, Modulatory effects of α7 nAChRs on the immune system and its relevance for CNS disorders, Cell. Mol. Life Sci. 73 (2016) 2511–2530, https://doi.org/10.1007/s00018-016-2175-4.
[11] J. Zhang, W. Yao, Q. Ren, C. Yang, C. Dong, M. Ma, J. Wu, K. Hashimoto, Depression-like phenotype by deletion of α7 nicotinic acetylcholine receptor: role of BDNF-TrkB in nucleus accumbens, Sci. Rep. 6 (2016) 36705.
[12] G. Scabia, R. Cancello, C. Dallanoce, S. Berger, C. Matera, A. Dattilo, A. Zulian, I. Barone, G. Ceccarini, F. Santini, M. De Amici, A.M. Di Blasio, M. Maffei, ICH3, a selective alpha7 nicotinic acetylcholine receptor agonist, modulates adipocyte inflammation associated with obesity, J. Endocrinol. Invest. 43 (2020), https://doi.org/10.1007/s40618-020-01182-z.
[13] W.J. Deal, B.F. Erlanger, D. Nachmansohn, Photoregulation of biological activity by photochromic reagents. 3. Photoregulation of bioelectricity by acetylcholine receptor inhibitors, Proc. Natl. Acad. Sci. 64 (1969) 1230–1234, https://doi.org/10.1073/pnas.64.4.1230.
[14] E. Bartels, N.H. Wassermann, B.F. Erlanger, Photochromic activators of the acetylcholine receptor, Proc. Natl. Acad. Sci. 68 (1971) 1820–1823, https://doi.org/10.1073/pnas.68.8.1820.
[15] I. Silman, A. Karlin, Acetylcholine receptor: covalent attachment of depolarizing groups at the active site, Science 164 (1979) (1969) 1420–1421, https://doi.org/10.1126/science.164.3886.1420.
[16] I. Tochitsky, M.R. Banghart, A. Mourot, J.Z. Yao, B. Gaub, R.H. Kramer, D. Trauner, Optochemical control of genetically engineered neuronal nicotinic acetylcholine receptors, Nat. Chem. 4 (2012) 105–111, https://doi.org/10.1038/nchem.1234.
[17] A. Damijonaitis, J. Broichhagen, T. Urushima, K. Hüll, J. Nagpal, L. Laprell, M. Schönberger, D.H. Woodmansee, A. Rafiq, M.P. Sumser, W. Kummer, A. Gottschalk, D. Trauner, AzoCholine enables optical control of alpha 7 nicotinic acetylcholine receptors in neural networks, ACS Chem. Neurosci. 6 (2015) 701–707, https://doi.org/10.1021/acschemneuro.5b00030.
[18] C. Dallanoce, F. Frigerio, G. Martelli, G. Grazioso, C. Matera, D.Y. Pomè, L. Pucci, F. Clementi, C. Gotti, M.D. Amici, Novel tricyclic Δ2-isoxazoline and 3-oxo-2-methyl-isoxazolidine derivatives: synthesis and binding affinity at neuronal nicotinic acetylcholine receptor subtypes, Bioorg. Med. Chem. 18 (2010)

4498–4508. ⟨https://www.scopus.com/inward/record.uri?eid=2-s2.0-77953323415&doi=10.1016%2fj.bmc.2010.04.065&partnerID=40&md5=a231ba288e78c9b251f1df2b2942c219⟩.
[19] C. Matera, M. Quadri, M. Sciaccaluga, D.Y. Pomè, F. Fasoli, M. De Amici, S. Fucile, C. Gotti, C. Dallanoce, G. Grazioso, Modification of the anabaseine pyridine nucleus allows achieving binding and functional selectivity for the α3β4 nicotinic acetylcholine receptor subtype, Eur. J. Med. Chem. 108 (2016) 392–405, https://doi.org/10.1016/j.ejmech.2015.11.045.
[20] M. Quadri, C. Matera, A. Silnović, M.C. Pismataro, N.A. Horenstein, C. Stokes, R. L. Papke, C. Dallanoce, Identification of α7 nicotinic acetylcholine receptor silent agonists based on the spirocyclic quinuclidine-Δ2-isoxazoline scaffold: synthesis and electrophysiological evaluation, ChemMedChem 12 (2017) 1335–1348. ⟨https://www.scopus.com/inward/record.uri?eid=2-s2.0-85028357080&doi=10.1002%2fcmdc.201700162&partnerID=40&md5=5c295e91808f134594f01a6c9db6b206⟩.
[21] C. Matera, G. Dondio, D. Braida, L. Ponzoni, M. De Amici, M. Sala, C. Dallanoce, vivo and in vitro ADMET profiling and in vivo pharmacodynamic investigations of a selective α7 nicotinic acetylcholine receptor agonist with a spirocyclic Δ2-isoxazoline molecular skeleton, Eur. J. Pharmacol. 820 (2018), https://doi.org/10.1016/j.ejphar.2017.12.047.
[22] J. Morstein, M. Awale, J.-L. Reymond, D. Trauner, Mapping the Azolog Space Enables the Optical Control of New Biological Targets (https://pubs.acs.org/doi/), ACS Cent. Sci. 5 (2019) 607–618, https://doi.org/10.1021/acscentsci.8b00881.
[23] F.T. Coppo, E.S.L. Maskell, S. Redshaw, J. Skidmore, R.W. Ward, D.M. Wilson, 2-Phenyl-5-amino-1,3,4-oxadiazoles and their use as nicotinic acetylcholine receptor ligands, WO2007138033A1, 2007.
[24] D.N. Hurst, N.P. King, S.Y. Mak, T. Scoccitti, J. Skidmore, Oxadiazole derivatives and their use as nicotinic acetylcholine receptor modulators, WO2009071577A1, 2009.
[25] D. Peters, D.B. Timmermann, E.Ø. Nielsen, E.D. Christoffersen, Novel 1,4-diaza-bicyclo[3.2.2]nonyl oxadiazolyl derivatives useful as modulator of nicotinic acetylcholine receptors, WO2009112460A1, 2009.
[26] M. Izquierdo-Serra, M. Gascón-Moya, J.J. Hirtz, S. Pittolo, K.E. Poskanzer, È. Ferrer, R. Alibés, F. Busqué, R. Yuste, J. Hernando, P. Gorostiza, Two-photon neuronal and astrocytic stimulation with azobenzene-based photoswitches (https://pubs.acs.org/doi/), J. Am. Chem. Soc. 136 (2014) 8693–8701, https://doi.org/10.1021/ja5026326.
[27] S. Pittolo, H. Lee, A. Lladó, S. Tosi, M. Bosch, L. Bardia, X. Gómez-Santacana, A. Llebaria, E. Soriano, J. Colombelli, K.E. Poskanzer, G. Perea, P. Gorostiza, Reversible silencing of endogenous receptors in intact brain tissue using 2-photon pharmacology (http://www.pnas.org/lookup/doi/), Proc. Natl. Acad. Sci. U. S. A. 116 (2019) 13680–13689, https://doi.org/10.1073/pnas.1900430116.
[28] F. Riefolo, C. Matera, A. Garrido-Charles, A.M.J. Gomila, R. Sortino, L. Agnetta, E. Claro, R. Masgrau, U. Holzgrabe, M. Batlle, M. Decker, E. Guasch, P. Gorostiza, Optical control of cardiac function with a photoswitchable muscarinic agonist, J. Am. Chem. Soc. 141 (2019) 7628–7636, https://doi.org/10.1021/jacs.9b03505.
[29] R. Sortino, M. Cunquero, G. Castro-Olvera, R. Gelabert, M. Moreno, F. Riefolo, C. Matera, N. Fernàndez-Castillo, L. Agnetta, M. Decker, J.M. Lluch, J. Hernando, P. Loza-Alvarez, P. Gorostiza, Three-photon infrared stimulation of endogenous neuroreceptors in vivo, Angew. Chem. - Int. Ed. 62 (2023) e202311181, https://doi.org/10.1002/anie.202311181.
[30] E.C. Carroll, S. Berlin, J. Levitz, M.A. Kienzler, Z. Yuan, D. Madsen, D.S. Larsen, E. Y. Isacoff, Two-photon brightness of azobenzene photoswitches designed for glutamate receptor optogenetics, Proc. Natl. Acad. Sci. 112 (2015), https://doi.org/10.1073/pnas.1416942112.
[31] M. Dudek, N. Tarnowicz-Staniak, M. Deiana, Z. Pokładek, M. Samoć, K. Matczyszyn, Two-photon absorption and two-photon-induced isomerization of azobenzene compounds, RSC Adv. 10 (2020) 40489–40507, https://doi.org/10.1039/D0RA07693G.
[32] S. Kellner, S. Berlin, Two-photon excitation of azobenzene photoswitches for synthetic optogenetics, Appl. Sci. 10 (2020) 805, https://doi.org/10.3390/app10030805.
[33] G. Cabré, A. Garrido-Charles, M. Moreno, M. Bosch, M. Porta-de-la-Riva, M. Krieg, M. Gascón-Moya, N. Camarero, R. Gelabert, J.M. Lluch, F. Busqué, J. Hernando, P. Gorostiza, R. Alibés, Rationally designed azobenzene photoswitches for efficient two-photon neuronal excitation, Nat. Commun. 10 (2019) 907–912. ⟨http://www.nature.com/articles/s41467-019-08796-9⟩.
[34] G.G. Spence, E.C. Taylor, O. Buchardt, The photochemical reactions of azoxy compounds, nitrones, and aromatic amine n-oxides, Chem. Rev. 70 (1970), https://doi.org/10.1021/cr60264a003.
[35] M.P. Faillace, J. Ortiz, L. Rocco, R. Bernabeu, Histone Methyltransferase G9a Plays an Essential Role on Nicotine Preference in Zebrafish, Mol. Neurobiol. 61 (2024) 6245–6263, https://doi.org/10.1007/s12035-024-03961-8.
[36] A. Pisera-Fuster, J. Zwiller, R. Bernabeu, Methionine Supplementation Abolishes Nicotine-Induced Place Preference in Zebrafish: a Behavioral and Molecular Analysis, Mol. Neurobiol. 58 (2021) 2590–2607, https://doi.org/10.1007/s12035-020-02260-2.
[37] L. Ponzoni, M.-T. Teh, J.V. Torres-Perez, C.H. Brennan, D. Braida, M. Sala, Increased Response to 3,4-Methylenedioxymethamphetamine (MDMA) Reward and Altered Gene Expression in Zebrafish During Short- and Long-Term Nicotine Withdrawal, Mol. Neurobiol. 58 (2021) 1650–1663, https://doi.org/10.1007/s12035-020-02225-5.
[38] F.X. Mora-Zamorano, K.R. Svoboda, M.J. Carvan, The nicotine-evoked locomotor response: a behavioral paradigm for toxicity screening in zebrafish (Danio rerio) embryos and eleutheroembryos exposed to methylmercury, PLoS. One 11 (2016), https://doi.org/10.1371/journal.pone.0154570.
[39] L.T. Thomas, L. Welsh, F. Galvez, K.R. Svoboda, Acute nicotine exposure and modulation of a spinal motor circuit in embryonic zebrafish, Toxicol. Appl. Pharmacol. 239 (2009), https://doi.org/10.1016/j.taap.2008.08.023.
[40] M. Rima, Y. Lattouf, M. Abi Younes, E. Bullier, P. Legendre, J.M. Mangin, E. Hong, Dynamic regulation of the cholinergic system in the spinal central nervous system, Sci. Rep. 10 (2020), https://doi.org/10.1038/s41598-020-72524-3.
[41] K.R. Svoboda, S. Vijayaraghavan, R.L. Tanguay, Nicotinic receptors mediate changes in spinal motoneuron development and axonal pathfinding in embryonic zebrafish exposed to nicotine, J. Neurosci. 22 (2002), https://doi.org/10.1523/jneurosci.22-24-10731.2002.
[42] Z. Bencan, E.D. Levin, The role of α7 and α4β2 nicotinic receptors in the nicotine-induced anxiolytic effect in zebrafish, Physiol. Behav. 95 (2008), https://doi.org/10.1016/j.physbeh.2008.07.009.
[43] J.M. Zirger, C.E. Beattie, D.B. McKay, R.T. Boyd, Cloning and expression of zebrafish neuronal nicotinic acetylcholine receptors, Gene Expr. Patterns 3 (2003), https://doi.org/10.1016/S1567-133X(03)00126-1.
[44] C. Matera, P. Calvé, V. Casadó-Anguera, R. Sortino, A.M.J. Gomila, E. Moreno, T. Gener, C. Delgado-Sallent, P. Nebot, D. Costazza, S. Conde-Berriozabal, M. Masana, J. Hernando, V. Casadó, M.V. Puig, P. Gorostiza, Reversible Photocontrol of Dopaminergic Transmission in Wild-Type Animals, Int. J. Mol. Sci. 23 (2022) 10114, https://doi.org/10.3390/ijms231710114.
[45] C.M. Noviello, A. Gharpure, N. Mukhtasimova, R. Cabuco, L. Baxter, D. Borek, S. M. Sine, R.E. Hibbs, Structure and gating mechanism of the α7 nicotinic acetylcholine receptor, Cell 184 (2021), https://doi.org/10.1016/j.cell.2021.02.049.
[46] Y. Zhao, S. Liu, Y. Zhou, M. Zhang, H. Chen, H. Eric Xu, D. Sun, L. Liu, C. Tian, Structural basis of human α7 nicotinic acetylcholine receptor activation, Cell. Res. 31 (2021), https://doi.org/10.1038/s41422-021-00509-6.
[47] C. Papotto, C. Stokes, C. Matera, S.M. Herz, K. Chiang, R. Ferrisi, M. De Amici, M. I. Damaj, R.L. Papke, C. Dallanoce, Sulfonium Moieties as Ammonium Bioisosteres: Novel Ligands for the Alpha7 Nicotinic Acetylcholine Receptor, J. Med. Chem. 68 (2025) 3157–3179, https://doi.org/10.1021/acs.jmedchem.4c02399.
[48] P. Wenig, J. Odermatt, OpenChrom: A cross-platform open source software for the mass spectrometric analysis of chromatographic data, BMC Bioinforma. 11 (2010), https://doi.org/10.1186/1471-2105-11-405.
[49] M.J. Frisch, G.W. Trucks, H.B. Schlegel, D.J. Fox, Gaussian 16 Revision A.03, (n. d.).
[50] J.C. Gordon, J.B. Myers, T. Folta, V. Shoja, L.S. Heath, A. Onufriev, H++: A server for estimating pKas and adding missing hydrogens to macromolecules, Nucleic Acids Res. 33 (2005), https://doi.org/10.1093/nar/gki464.
[51] A. Pedretti, A. Mazzolari, S. Gervasoni, L. Fumagalli, G. Vistoli, The VEGA suite of programs: an versatile platform for cheminformatics and drug design projects, Bioinformatics 37 (2021) 1174–1175, https://doi.org/10.1093/bioinformatics/btaa774.